JOURNAL OF PETROLOGY

Journal of Petrology, 2021, Vol. 62, No. 10, 1–29
doi: 10.1093/petrology/egab053
Advance Access Publication Date: 18 June 2021
Original Manuscript

OXFORD

Textural and Geochemical Evidence for Magnetite Production upon Antigorite Breakdown During Subduction

Joana F. Vieira Duarte *, Francesca Piccoli, Thomas Pettke and Jörg Hermann

Institute of Geological Sciences, University of Bern, Baltzerstrasse 3, Bern, 3012, Switzerland

*Corresponding author. Telephone: +41 (0)31 631 89 74. E-mail: joana.vieira@geo.unibe.ch

Received 29 October 2020; Accepted 8 June 2021

ABSTRACT

Magnetite stability in ultramafic systems undergoing subduction plays a major role in controlling redox states of the fluids liberated upon dehydration reactions, as well as of residual rocks. Despite their relevance for the evaluation of the redox conditions, the systematics and geochemistry of oxide minerals have remained poorly constrained in subducted ultramafic rocks. Here, we present a detailed petrological and geochemical study of magnetite in hydrous ultramafic rocks from Cerro del Almirez (Spain). Our results indicate that prograde to peak magnetite, ilmenite–hematite solid solution minerals, and sulfides coexist in both antigorite-serpentinite and chlorite-harzburgite at *c.* 670 °C and 1·6 GPa, displaying successive crystallization stages, each characterized by specific mineral compositions. In antigorite-serpentinite, magnetite inherited from seafloor hydration and recrystallized during subduction has moderate Cr ($Cr_2O_3 < 10$ wt%) and low Al and V concentrations. In chlorite-harzburgite, polygonal magnetite is in textural equilibrium with olivine, orthopyroxene, chlorite, pentlandite, and ilmenite–hematite solid solution minerals. The Cr_2O_3 contents of this magnetite are up to 19 wt%, higher than any magnetite data obtained for antigorite-serpentinite, along with higher Al and V, derived from antigorite breakdown, and lower Mn concentrations. This polygonal magnetite displays conspicuous core to rim zoning as recognized on elemental maps. Cr–V–Al–Fe^{3+} mass-balance calculations, assuming conservative behavior of total Fe^{3+} and Al, were employed to model magnetite compositions and modes in the partially dehydrated product chlorite-harzburgite starting from antigorite-serpentinite, as well as in the serpentinite protolith starting from the chlorite-harzburgite. The model results disagree with measured Cr and V compositions in magnetite from antigorite-serpentinites and chlorite-harzburgites. This indicates that these two rock types had different initial bulk compositions and thus cannot be directly compared. Our mass-balance analysis also reveals that new magnetite formation is required across the antigorite-breakdown reaction to account for the mass conservation of fluid-immobile elements such as Cr–V–Al–Fe^{3+}. Complete recrystallization and formation of new magnetite in equilibrium with peak olivine (Mg# 89–91), chlorite (Mg# ~95), orthopyroxene (Mg# 90–91), and pentlandite buffer the released fluid to redox conditions of ~1 log unit above the quartz–fayalite–magnetite buffer. This is consistent with the observation that the Fe–Ti solid solution minerals (hemo-ilmenite and ilmeno-hematite) crystallized as homogeneous phases and exsolved upon exhumation and cooling. We conclude that antigorite-dehydration reaction fluids carry only a moderate redox budget and therefore may not be the only reason why the magmas are comparatively oxidized.

Key words: magnetite; redox conditions; antigorite breakdown; Cerro del Almirez; LA-ICP-MS

INTRODUCTION

Magnetite is a very common accessory mineral forming upon hydrothermal alteration of peridotite (i.e. serpentinization; Cannat *et al.*, 1992; Cannat, 1993). The presence of magnetite in serpentinites is important for many geological processes occurring both at shallow and at deep levels. Magnetite formation at slow-spreading ridges (i.e. oceanic serpentinites) has mostly been investigated for its relevance for the emergence of life on Earth (Sleep *et al.*, 2004; Martin *et al.*, 2008; Ménez *et al.*, 2018) and its contribution to the magnetic properties of oceanic lithosphere (Bina & Henry, 1990; Toft *et al.*, 1990; Dyment *et al.*, 1997; Oufi *et al.*, 2002; Maffione *et al.*, 2014). Serpentinization and magnetite formation can also occur during subduction, where aqueous fluids, released from the slab, infiltrate and hydrate the mantle wedge (e.g. Vitale Brovarone *et al.*, 2020), or during slab bending (Ranero *et al.*, 2003). The mantle wedge serpentinization can contribute to long-wavelength magnetic anomalies above subduction zones (e.g. Blakely *et al.*, 2005).

The fate of magnetite during subduction metamorphism has been addressed in several studies. The reason behind this interest is that the possible magnetite breakdown during subduction may produce oxidized fluids that can, ultimately, account for the oxidized nature of arc lavas (Kelley & Cottrell, 2009; Brounce *et al.*, 2015; Evans *et al.*, 2017; Evans & Frost, 2021). Nevertheless, the role of magnetite in metamorphic dehydration reactions as reactant or product mineral is a matter of controversy. Magnetite is preserved during the first subduction-related dehydration of antigorite + brucite = olivine + chlorite + H_2O in serpentinites from Erro Tobbio (e.g. Peters *et al.*, 2020) and Zermatt–Saas (Kempf *et al.*, 2020). On the other hand, it has been proposed that during the antigorite-dehydration reaction magnetite is consumed, and thus redox budget can be transferred from the rock to the fluids (e.g. Debret *et al.*, 2015; Evans *et al.*, 2017). However, this vision has been challenged by the observation that when magnetite is present, fluids are released at rock-buffered conditions and do not carry a significant redox budget, as based on natural samples and/or thermodynamic modeling (Piccoli *et al.*, 2019; Lazar, 2020; Evans & Frost, 2021), and experimental evidence (Iacovino *et al.*, 2020). The mode of magnetite in high-pressure serpentinites depends on the degree of ocean-floor serpentinization of the protolith (e.g. Andreani *et al.*, 2013), which in turn depends on the geodynamic setting (Klein *et al.*, 2014; Evans *et al.*, 2017; Mothersole *et al.*, 2017). A crucial point that so far has never been addressed in subducted abyssal serpentinites is that, depending on the protolith, magnetite abundance inherited from oceanic alteration can vary widely, ranging from more than 6 wt% to nearly zero (Whittaker & Wicks, 1970; Seyfried *et al.*, 2007; Evans, 2008; Beard *et al.*, 2009; Andreani *et al.*, 2013; Klein *et al.*, 2014; Bonnemains *et al.*, 2016). Therefore, it is impossible to know *a priori* the initial magnetite content of metamorphic serpentinites and thus it is impossible to state if magnetite is consumed by relying only on its abundances in rocks of different metamorphic degrees from various localities. Another possibility that has not been explored yet is if magnetite could actually be formed during dehydration reactions involving antigorite and chlorite that hosts some ferric iron (e.g. Evans *et al.*, 2012; Debret *et al.*, 2015; Evans & Frost, 2021).

A large number of minor and trace elements can substitute into magnetite, and characteristic geochemical signatures can be used as petrogenetic indicators (e.g. Dare *et al.*, 2014; Colás *et al.*, 2016). However, this very promising geochemical tool has remained completely unexplored for magnetite in metamorphic serpentinites from subduction settings. In particular, despite the importance of magnetite for subduction-zone processes, there are no trace geochemical data available in the literature for magnetite from subducted serpentinites.

Here we propose a novel approach to unveil the fate of magnetite during dehydration reactions in subducting serpentinites, to understand if it is produced or consumed. We investigated in great detail the petrological and geochemical systematics of magnetite and ilmenite–hematite solid solution formed upon ocean-floor hydration and prograde subduction metamorphism, which discloses important insight into mineral growth during continued metamorphism. We used diverse antigorite-serpentinite (hereafter, Atg-serpentinite) and chlorite-harzburgite (hereafter, Chl-harzburgite) samples coexisting in the field from Cerro del Almirez (Spain), subducted to ~50 km depth, and focused on the antigorite-dehydration reaction. We demonstrate that magnetite is stable throughout all ultramafic rock types, well beyond antigorite-dehydration in Chl-harzburgite. Compositional differences between magnetite from Chl-harzburgite and Atg-serpentinite demonstrate that Atg-serpentinite cannot be considered as precursor rock of Chl-harzburgite (i.e. the protoliths of the two lithologies were different). In addition, the geochemical signature of magnetite from Chl-harzburgite indicates that precursor magnetite recrystallized, and new magnetite formed along with the products olivine, orthopyroxene, and chlorite in response to antigorite dehydration. Our findings indicate that fluids produced during the antigorite-dehydration reaction may transport only moderate redox budget, thus possibly requiring additional contributions to account for the rather oxidized nature of arc magmas.

GEOLOGICAL SETTING

The ultramafic massif of the Cerro del Almirez (Fig. 1) forms part of the Mulhacén Unit, the upper sequence of the Nevado–Filábride Complex of the Betic Cordillera, Spain, which represents exhumed slices of the western branch of the Piemont–Ligurian Ocean (Trommsdorff

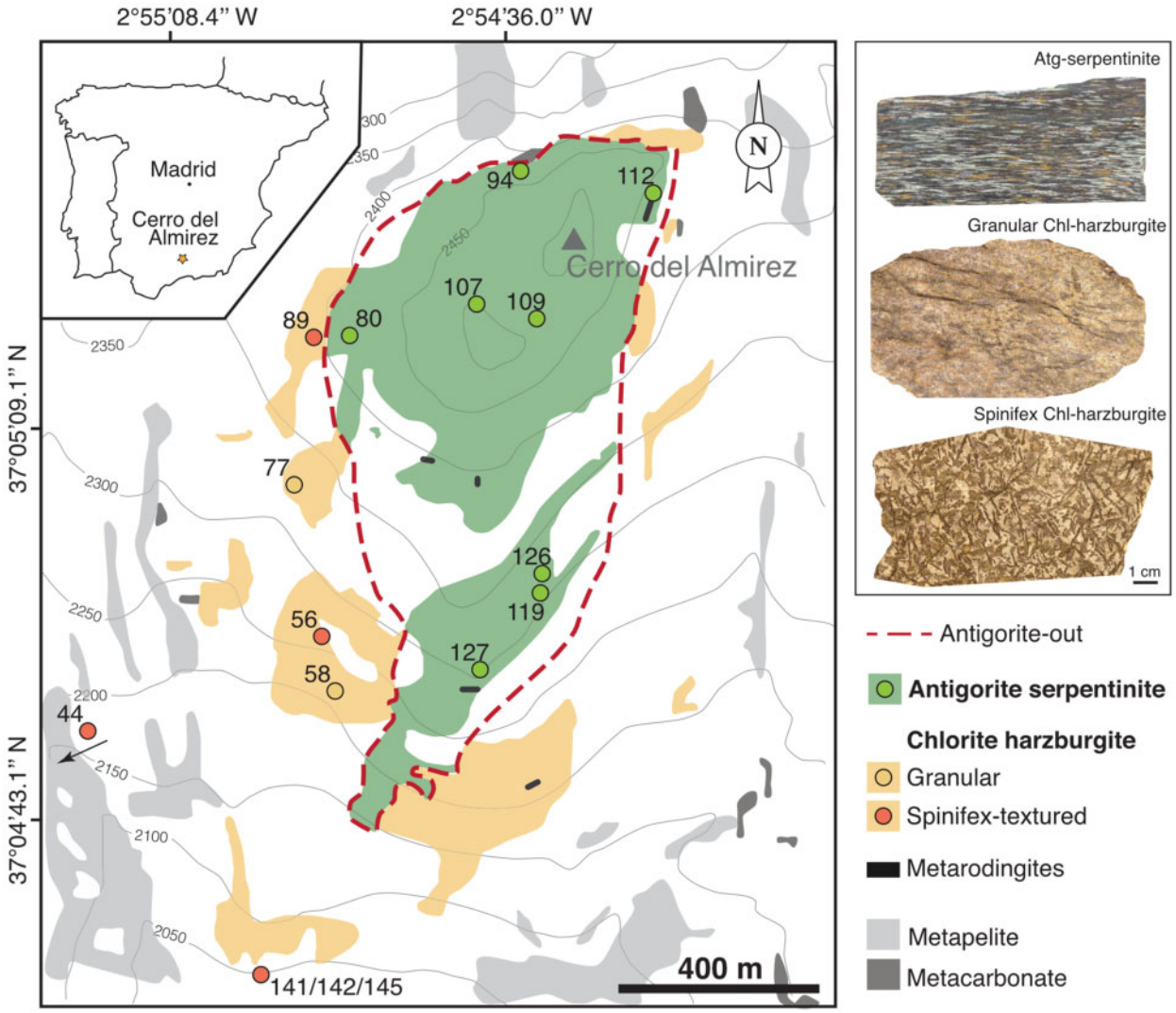

Fig. 1. Location of the Cerro del Almirez in the Betic Cordillera (Spain) and geological map (modified Schönbächler, 1999; Bretscher *et al.*, 2018). Dashed red line represents the antigorite-out boundary, separating Atg-serpentinite from Chl-harzburgite along a primary contact. Sample types and locations are indicated by colored circles. Hand samples for the main ultramafic lithologies are illustrated to the right (from top to bottom): Atg-serpentinite, granular and spinifex-textured Chl-harzburgite. Images show weathered sample surfaces to illustrate olivine modes.

et al., 1998; Puga *et al.*, 1999). Ultramafic rocks occur intercalated with metasediments (i.e. quartzites, micaschists, and marbles) and, locally, orthogneisses (Schönbächler, 1999). The oceanic origin of the Almirez hydrous mantle rocks is demonstrated by the occurrence of meta-rodingites (Trommsdorff *et al.*, 1998; Laborda-López *et al.*, 2018), by specific trace element systematics (e.g. Scambelluri *et al.*, 2004; Peters *et al.*, 2017), and by H–C–O–S isotopic compositions (Alt *et al.*, 2012). Oceanic serpentinites underwent subduction and reached peak metamorphic conditions of ~650–700 °C and peak pressures between 1·6 and 1·9 GPa in the middle Miocene (López Sánchez-Vizcaíno *et al.*, 2001; Padrón-Navarta *et al.*, 2010). These have recently been refined to ~670 °C and 1·6 GPa based on the reactive bulk Mg# of silicate minerals, and coexistence of Atg-serpentinites and Chl-harzburgites (Bretscher *et al.*, 2018). During this event, parts of the subducted Atg-serpentinites were transformed to prograde Chl-harzburgite via antigorite breakdown reaction (Trommsdorff *et al.*, 1998). The contact between Atg-serpentinite and Chl-harzburgite is tectonically undisturbed and discordant to the main foliation, hence it is considered as a primary contact (Fig. 1; Trommsdorff *et al.*, 1998; Padrón-Navarta *et al.*, 2011). It has been proposed that the preserved antigorite-dehydration reaction front formed following the direction of the heat flux (Padrón-Navarta *et al.*, 2011), and the volume of unreacted Atg-serpentinites might be due to either tectonic forcing (i.e. where buoyancy forces outweigh drag forces during subduction; Garcia-Casco *et al.*, 2002; Gerya & Stöckhert, 2006) or variation of intensive parameters controlled by the hydrodynamics of fluids released by dehydration (Connolly & Thompson, 1989;

Lyubetskaya & Ague, 2009). More recently, it has been proposed that the dehydration front rather represents a compositional boundary; that is, an oxidation front imposed upon serpentinization at the ocean floor (Bretscher *et al.*, 2018).

Field relations and sampling

The studied rock types include variably foliated Atg-serpentinites, and granular- and spinifex-textured Chl-harzburgites (Fig. 1). Antigorite-serpentinites consist of an antigorite-rich matrix with metamorphic clinopyroxene, olivine, tremolite, magnetite, and sulfides; texturally, the only mantle relic mineral is scattered clinopyroxene (Trommsdorff *et al.*, 1998; Padrón-Navarta *et al.*, 2010, 2011; Bretscher *et al.*, 2018). The Chl-harzburgites display a common prograde equilibrium assemblage composed of olivine, orthopyroxene, and chlorite along with magnetite and sulfides. The granular- and spinifex-textured Chl-harzburgites differ from each other texturally, the spinifex-textured type being characterized by long olivine crystals with brown oxide-rich rims, along with interstitial chlorite, orthopyroxene, olivine, and oxides plus minor sulfides. In the samples investigated in detail for this study, we did not observe Ti-clinohumite, although it has been reported in previous studies from Cerro del Almirez (e.g. Trommsdorff *et al.*, 1998; López Sánchez-Vizcaíno *et al.*, 2005; Padrón-Navarta *et al.*, 2011; Bretscher *et al.*, 2018). Retrogression is variably prominent and addressed in detail below.

METHODS

Detailed petrography was determined for 16 samples by transmitted and reflected light microscopy, aided by Raman spectroscopy, and scanning electron microscopy (SEM). Textures and opaque mineral modes were estimated by image processing of high-resolution reflected light scans obtained by multiple image alignment (MIA scan). *In situ* measurements for major and trace elements of oxide minerals were performed by electron probe microanalysis (EPMA) and laser ablation inductively coupled plasma mass spectrometry (LA-ICP-MS).

MIA scan

Multiple image alignment scans of thin sections were produced using an Olympus BX51 microscope equipped with a motorized stage and camera, remotely controlled by Olympus Stream Motion (version 1.8 software). Images were acquired in reflected light, at maximum light intensity and using a 5× magnification lens. Acquisition parameters were manually adjusted at constant exposure time of 500 μs, ISO of 200, and using a stitching overlap of 20%. Final images were exported in TIFF format and compressed to 30% to allow image post-processing with ImageJ software (Schneider *et al.*, 2012). Here, images were converted to 8-bit and area selections corresponding to oxide and sulfide phases were created using grey-scale threshold intervals (ranging from 90 to 143, and from 143 to 234 for oxides and sulfides, respectively). The estimated image resolution of this method is *c.* 5 μm, implying that sulfides and oxides with smaller size (e.g. the exsolutions from brown olivine and those lining retrograde mesh serpentine) were not accounted for in calculated modes; hence, opaque mineral modes represent minimum estimates.

Electron probe microanalysis

Spot measurements

Electron probe microanalysis (EPMA) measurements were performed for magnetite, pentlandite, and pyrrhotite from Atg-serpentinite and Chl-harzburgite samples. Major and minor element abundances in oxide minerals were determined by wavelength-dispersive spectrometry (WDS) using a JEOL JXA 8200 superprobe at the Institute of Geological Sciences, University of Bern, operated with an acceleration voltage of 15 kV, a probe current of 100 nA with a beam diameter of 10 μm, to prevent sample overheating. High probe current lowers the limits of detection (LOD) of minor elements (Al, Ti, Zn, Cr, Ni; Dupuis & Beaudoin, 2011). A beam size of 2 μm and probe current of 20 nA were used for ~5–10 μm oxide inclusions in porphyroblasts of olivine, orthopyroxene, and chlorite. The mass fractions of eight element oxides were calibrated using synthetic and natural standards: almandine (FeO), chromium spinel (Cr_2O_3; Al_2O_3), olivine (MgO), tephroite (MnO), nickel oxide (NiO), zinc oxide (ZnO), rutile (TiO_2). Ferric iron in magnetite was calculated by charge balance from stoichiometric compositions.

EPMA measurements of sulfides were performed at the Institute of Geological Sciences, University of Bern, and at the Institute of Geochemistry and Petrology of the ETH Zurich, with a JEOL JXA-8200 superprobe, operated with an acceleration voltage of 15 kV, a probe current of 20 nA and using a beam diameter of 2 μm. The mass fractions of six elements were calibrated using synthetic and natural standards: pyrite (Fe, S), pentlandite (Ni, Co), galena (Pb), chalcopyrite (Cu).

Element mapping of magnetite

Compositional maps were performed on magnetite from the Atg-serpentinite and from Chl-harzburgite, employing the same electron probe instrument and the analytical procedures as given by Lanari *et al.* (2014). The analytical conditions were 15 kV accelerating voltage, 100 nA probe current and dwell times of 200 ms. The sizes of the maps were 600 × 400 μm and 400 × 200 μm in the Atg-serpentinite and Chl-harzburgite samples, respectively. Elemental maps include Mg, Fe, Al, Ti, Cr, Ni, and Mn acquired in WDS mode, and V and Zn acquired in energy-dispersive spectrometry (EDS) mode. Data processing and calibration were performed using XMapTools 3.2.2 (Lanari

Table 1: Summary table of studied samples reporting mineral assemblages and modal abundances of opaque phases

Lithology	Sample	Mineral assemblage	Modal abundance (vol%)		
			Oxides	Sulfides	Total
Atg-serpentinite	Alm06-119	Atg, Ol, met. Cpx, Trem, Ti-Chu, **Mag**, **Pn**	0·92	0·07	0·99
	Alm06-112	Atg, Ol, met. Cpx, Trem, Ti-Chu, **Mag**, **Pn**	1·47	0·06	1·53
	Alm06-126	Atg, Ol, met. Cpx, relic Cpx, Ti-Chu, **Mag**, **Pn**	2·13	0·16	2·29
	Alm06-109	Atg, Ol, Chl, met. Cpx, relic Cpx, Ti-Chu, **Mag**, **Pn**	2·30	0·11	2·41
	Alm06-127	Atg, Ol, met. Cpx, relic Cpx, Trem, **Mag**, **Pn**	2·38	0·03	2·41
	Alm06-80	Atg, Ol, met. Cpx, relic Cpx, Trem, **Mag**, **Hem–Ilm**, **Pn**	2·41	0·04	2·45
	Alm06-107	Atg, Ol, Chl, met. Cpx, relic Cpx, Trem, **Mag**, **Pn**	3·12	0·10	3·22
	Alm06-94	Atg, Ol, Chl, met. Cpx, relic Cpx, Ti-Chu, **Mag**, **Pn**	3·83	0·04	3·87
Chl-harzburgite (granular-textured)	Alm06-58	Ol, Opx, Chl, Tlc, Lz, **Mag**, **Hem–Ilm**, **Pn**, **Po**	1·55	0·19	1·74
	Alm06-77	Ol, Opx, Chl, Tlc, Mgs, Lz, **Mag**, **Hem–Ilm**, **Pn**, **Po**	1·90	0·14	2·04
Chl-harzburgite (spinifex-textured)	Alm06-89	Ol, Opx, Chl, Trem, Tlc, **Mag**, **Pn**	0·06	0·09	0·15
	Alm06-56	Ol, Opx, Chl, Trem, Tlc, Lz, **Mag**, **Ilm–Hem**, **Pn**	0·31	0·13	0·44
	Alm06-44	Ol, Opx, Chl, Tlc, Lz, **Mag**, **Ilm–Hem**, **Pn**, **Po**	0·32	0·13	0·45
	Alm06-145a	Ol, Opx, Chl, Trem, Tlc, Lz, **Mag**, **Ilm–Hem**, **Pn**	0·94	0·03	0·97
	Alm06-141a	Ol, Opx, Chl, Trem, Tlc, Lz, **Mag**, **Ilm–Hem**, **Pn**	1·41	0·03	1·44
	Alm06-142a	Ol, Opx, Chl, Tlc, Lz, **Mag**, **Ilm–Hem**, **Pn**	3·49	0·03	3·52

Modal abundances of opaque minerals (indicated in bold type) were determined by MIA scan, assuming one-to-one relation of area per cent equals volume per cent. Samples are ordered by increasing oxide content for each lithology to emphasize oxide mode variability.

et al., 2014, 2019). The internal analytical standardization was performed using *in situ* spot analyses acquired on the same area.

LA-ICP-MS

Major to trace element concentrations of oxide minerals were measured by LA-ICP-MS at the Institute of Geological Sciences, University of Bern, Switzerland, employing a Resonetics RESOlutionSE 193 nm excimer laser system equipped with an S-155 large volume constant geometry ablation cell (Laurin Technic, Australia) coupled to an Agilent 7900 quadrupole ICP-MS system. The ICP-MS system was tuned for low oxide production (ThO/Th $< 0{\cdot}2$ %) and Th/U sensitivity ratio close to one (Th/U > 97 %). Ablation was performed in ultra-pure He ($0{\cdot}45\,l\,min^{-1}$) and N_2 ($0{\cdot}003\,l\,min^{-1}$) and the aerosol-bearing gas was mixed with Ar ($0{\cdot}86\,l\,min^{-1}$) prior to exiting the ablation cell. We employed a laser repetition rate of 7 Hz and $3\,J\,cm^{-2}$ fluence on sample.

The beam size was set to between 16 and 38 μm depending on grain size, and the surface area of each measurement spot was cleaned by pre-ablation for three pulses employing a slightly larger beam size. Total acquisition time for each measurement was ~100 s, consisting of 30–50 s of gas background acquired with the laser switched off, 10 s of washout after pre-ablation, and 30 s of sample signal.

Spot measurement data reduction was performed by using the software Iolite (Hellstrom *et al.*, 2008; Paton *et al.*, 2011). Instrument drift was corrected for by applying a step-forward spline-type function fit between interspersed sets of standard measurement spots. Quantification was performed using the trace element doped basaltic glass GSD-1g for external standardization [employing the preferred values listed by Peters & Pettke (2017)] and by internal standardization to 100 wt% element oxides [MgO, FeO, Cr_2O_3, Al_2O_3, TiO_2, MnO, NiO, V_2O_5, ZnO normalized to 100 % (m/m); Beta_TE_Norm reduction scheme in Iolite Igor Pro, version 7.08]. For the magnetite and hematite–ilmenite solid solution minerals, $X Fe^{3+}$ was calculated by stoichiometry of the respective oxides, thus returning concentration data for FeO and Fe_2O_3. Stringent LODs were calculated with the formulations detailed by Pettke *et al.* (2012).

RESULTS

Petrography

Rock oxide and sulfide mineral associations and their characteristic microtextures are presented in relationship to the silicate parageneses as described by Bretscher *et al.* (2018). Oxide and sulfide modes determined by MIA scan are reported in Table 1. Ocean-floor and prograde to peak mineral assemblages are described first, followed by retrogression features. Results are summarized in Fig. 2, and mineral abbreviations follow the nomenclature of Whitney & Evans (2010).

Ocean-floor to peak metamorphic oxide and sulfide crystallization

Magnetite is present in all samples from both lithologies, Atg-serpentinite and Chl-harzburgite, at highly variable modes (Table 1). Different magnetite populations were recognized on the basis of grain size and textural position. Here we report all the identified populations grouped by lithology.

In the Atg-serpentinite, three magnetite populations were recognized: (1) large anhedral grains; (2) small grains in the matrix; (3) small magnetite inclusions in silicates.

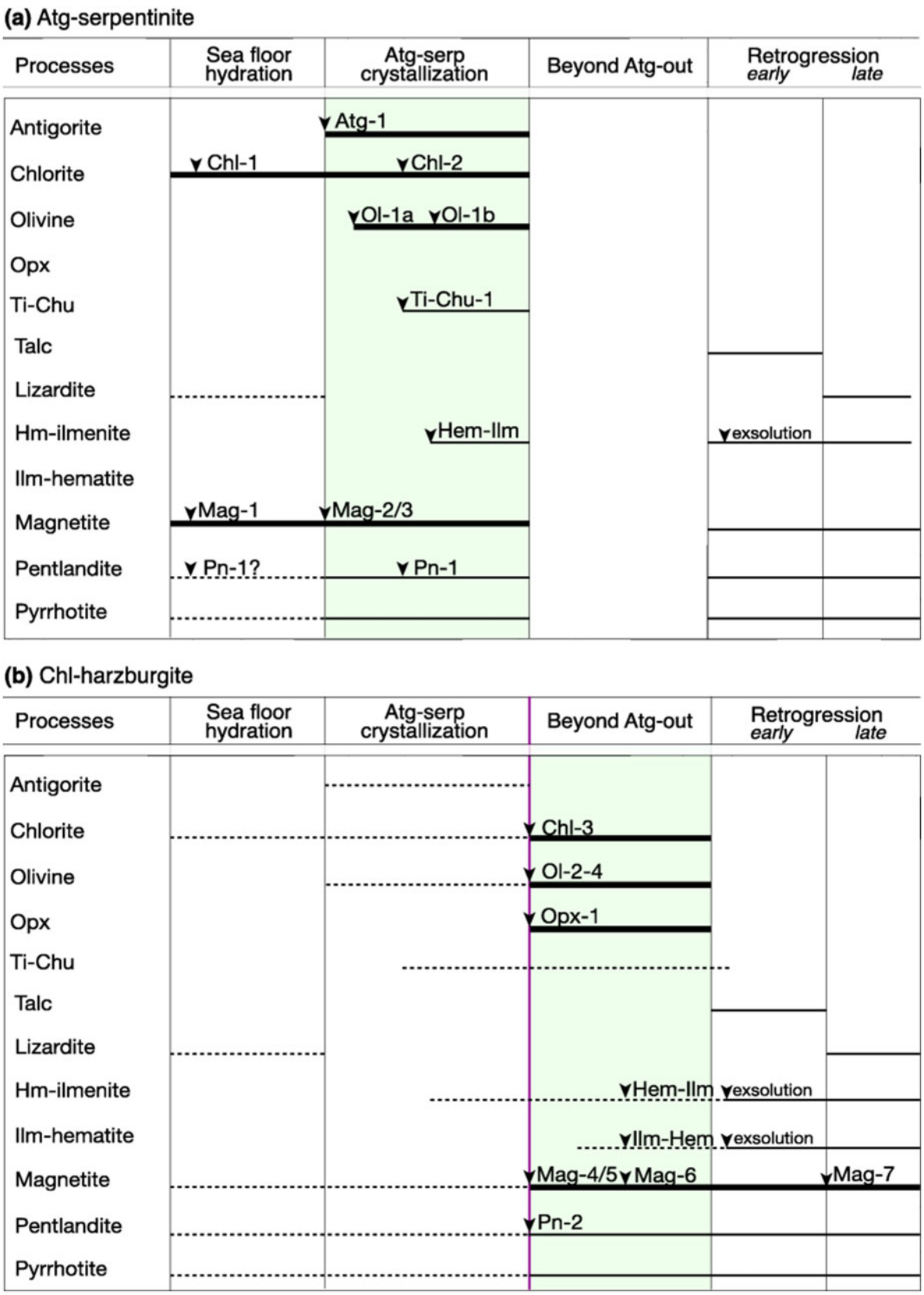

Fig. 2. Paragenetic sequence of mineral growth in (a) Atg-serpentinite and (b) Chl-harzburgite, after the antigorite-dehydration reaction. Silicate systematics is simplified after Bretscher *et al.* (2018) and extended for the opaque and retrograde assemblages. It should be noted that subordinate diopside, tremolite, and occasional carbonate were omitted for simplicity, as well as brucite (its former existence is implied by presence of Ol-1a). Dashed lines represent implied occurrences. Thick lines emphasize mineral assemblage relevant for constraining rock-buffered fO_2 conditions.

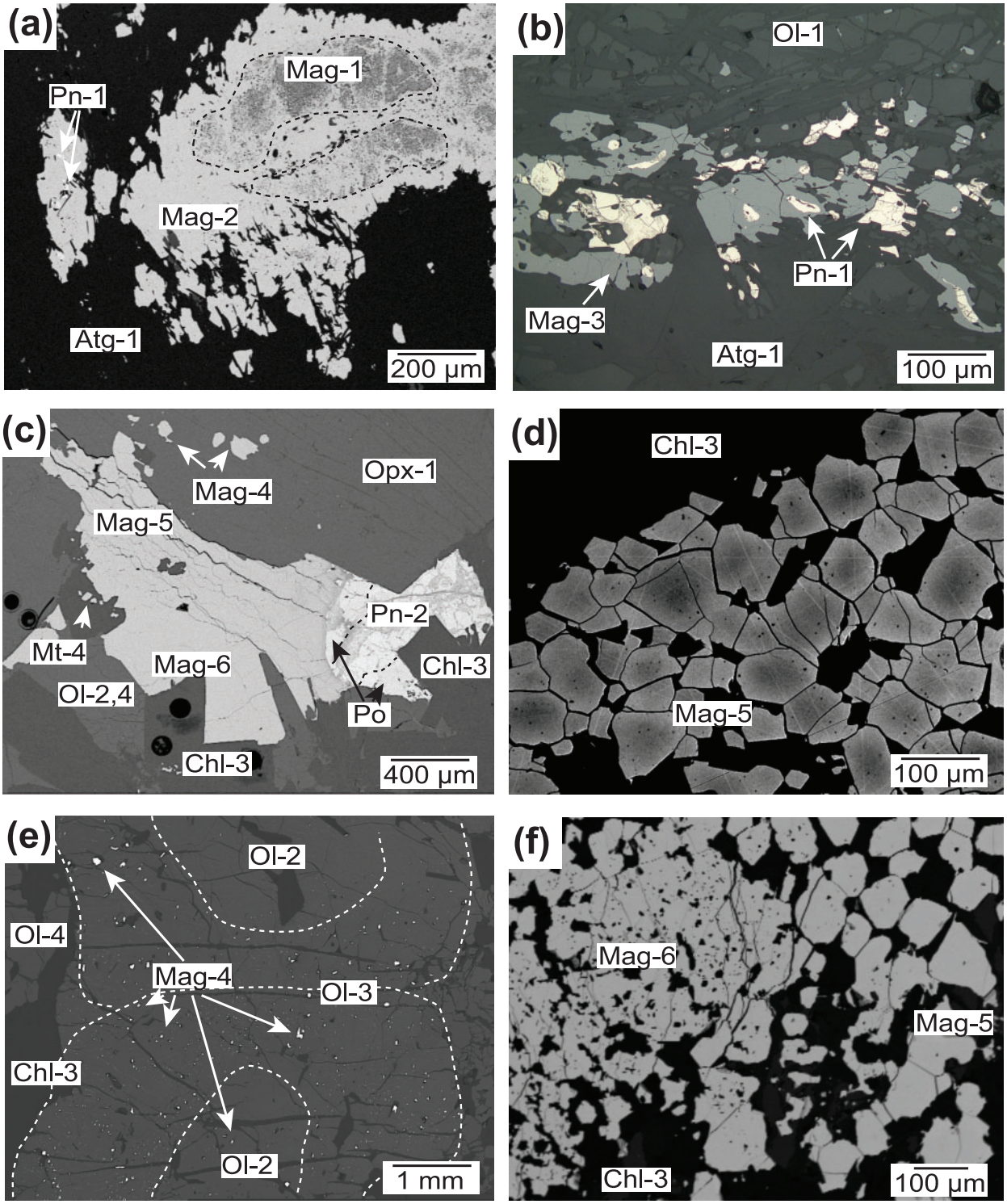

Fig. 3. Microtextures of magnetite, sometimes associated with pentlandite and pyrrhotite in (a, b) Atg-serpentinite, (c, d) granular-textured and (e, f) spinifex-textured Chl-harzburgite. (b) is a reflected light microscopy image; the others are BSE images. Black circles in (c) are LA-ICP-MS measurement craters.

Type (1) magnetite occurs as anhedral large grains ranging from 100 μm to 1 cm in size (Mag-1 and Mag-2, Fig. 3a). These magnetite crystals (Fig. 3a) are characterized by inclusion-rich cores (Mag-1), containing serpentine, clinopyroxene, and rare 5–20 μm sulfide inclusions, and by inclusion-free rims (Mag-2). Backscattered electron (BSE) images show a sharp transition between core and rim.

Type (2) magnetite forms small grains (≤100 μm) in the matrix, along the antigorite foliation (Mag-3,

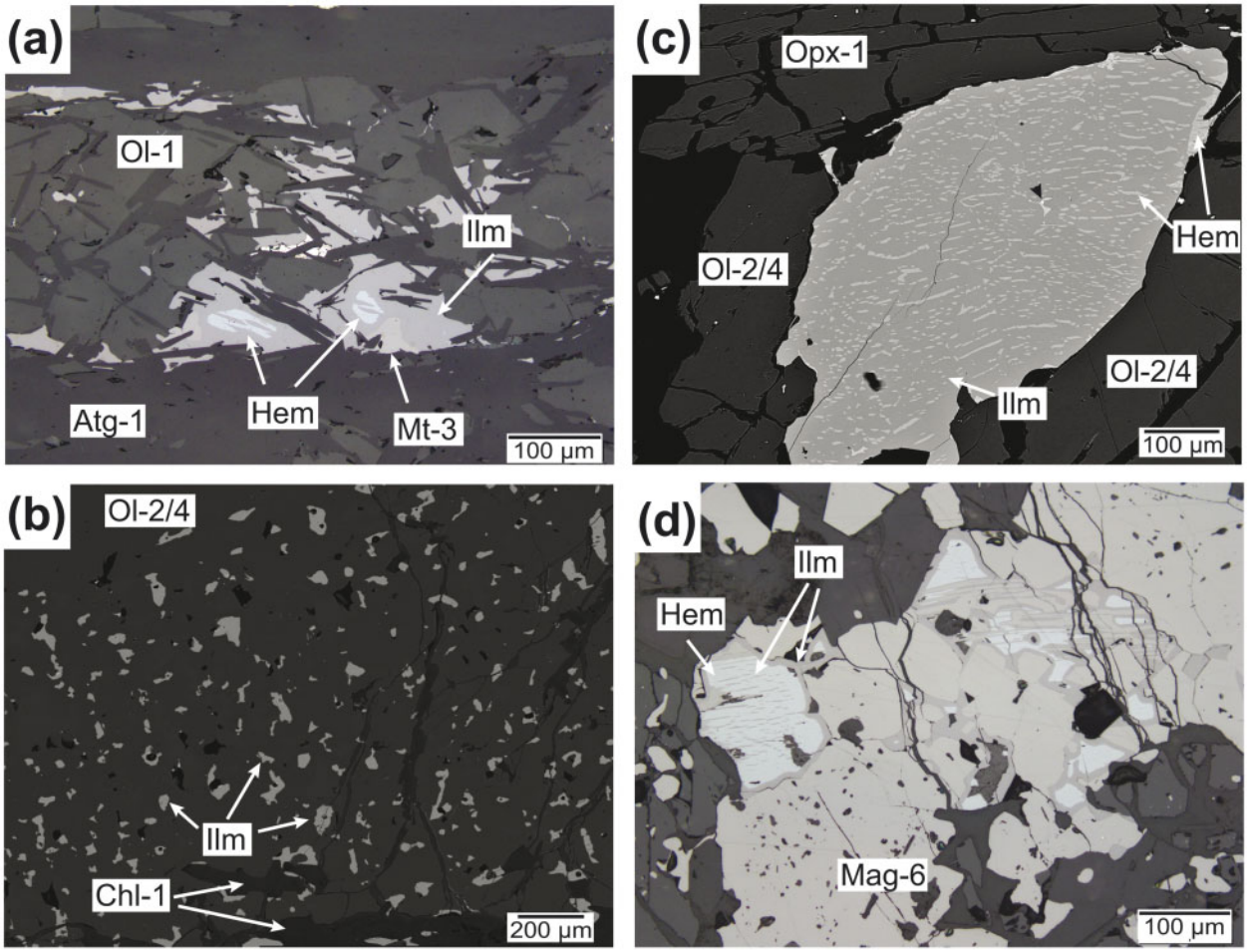

Fig. 4. Distinct textural types of ilmenite and intergrowths of ilmenite–hematite–magnetite, in (a) Atg-serpentinite, and both (b, c) granular-textured and (d) spinifex-textured Chl-harzburgite. Images (a) and (c) show distinct hemo-ilmenite exsolution (Hem-Ilm) textures; (b) intergrowths of ilmenite within Ol-2/4; (d) ilmeno-hematite (Ilm-Hem) textures. (a) and (d) are reflected light microscopy images; (b) and (c) are BSE images.

Fig. 3b). All crystals are inclusion-free and locally form intergrowths with pentlandite, both overgrown by antigorite blades.

Type (3) magnetite occurs as inclusions in silicates, lining exsolution lamellae in relic mantle clinopyroxene, tracing mantle pseudomorphs such as bastite and mesh texture, and as unoriented inclusions in prograde metamorphic olivine.

In the granular- and spinifex-textured Chl-harzburgite, three distinct magnetite populations were identified.

The first population represents magnetite inclusions in the antigorite-dehydration products olivine, orthopyroxene, and chlorite (Mag-4 in Fig. 3c and e).

The second population comprises 50-100 μm sizere-crystallized polygonal aggregates, sometimes forming clusters up to *c.* 1 cm (Mag-5 in Fig. 3c and d). Individual crystals are poor in inclusions and are zoned in BSE images, becoming increasingly brighter towards the rim (Mag-5, Fig. 3d). Some grains contain chlorite inclusions.

A third magnetite population (Mag-6 in Fig. 3c) is inclusion free and locally overgrows the polygonal aggregates (Mag-5). This last population displays sharp boundaries with olivine, orthopyroxene, and chlorite (Fig. 3c). In spinifex-textured samples, Mag-6 overgrowing polygonal Mag-5 shows characteristic spongy texture, intergrown with chlorite (Fig. 3f).

Ilmenite, hemo-ilmenite and ilmeno-hematite solid solution minerals are present in the Atg-serpentinite and Chl-harzburgite, subordinate to magnetite (Fig. 4).

In the Atg-serpentinite, only hemo-ilmenite occurs (<1 vol% of total oxides), in association with metamorphic olivine and magnetite (Mag-3). Hemo-ilmenite grains consist of ~100 μm ilmenite grains, with discontinuous and irregular hematite lamellae in the core (Fig. 4a).

In the Chl-harzburgite, wormy ilmenite and both hemo-ilmenite and ilmeno-hematite were observed. Rare wormy ilmenite (<1 vol% of total oxides) occurs in granular-textured samples as inclusions of *c.* 50 μm in rims of olivine (Fig. 4b) or in Mag-6. Hemo-ilmenite (~4 vol% of total oxides) was observed in granular-textured Chl-harzburgite as interstitial grains up to

200 μm mostly associated with metamorphic olivine (Ol-2/4, in Fig. 2) and chlorite (Chl-2), displaying fine (<10 μm) hematite exsolutions (Fig. 4c). The fraction of ilmenite in hematite was estimated by image analysis and is of the order of 85–90 %. Ilmeno-hematite (~4 vol% of total oxides) was observed in spinifex-textured Chl-harzburgite. Grains are up to 100 μm in size, are associated with larger Mag-6 grains, and display ilmenite lamellae in hematite and an ~10 μm ilmenite mantle (Fig. 4d). Image analysis returned a fraction of ilmenite in hematite ranging from 25 to 55 %, including mantling ilmenite.

Importantly, hematite was never found as isolated grains coexisting with magnetite in any lithology.

Pentlandite and pyrrhotite were the two sulfides observed. In the Atg-serpentinite, pentlandite (Pn-1) occurs as inclusions of *c.* 5–10 μm in Mag-1 (Fig. 3a) along with antigorite and clinopyroxene inclusions (identified by EDS), or as anhedral grains of up to ~100 μm in the antigorite matrix, forming intergrowths with Mag-3 (Fig. 3b). Minor pyrrhotite occurs as micrometer-sized zones within matrix pentlandite.

In the granular-textured Chl-harzburgite, pentlandite (Pn-2) was found in three distinct microtextural positions: (1) as large subhedral grains up to 500 μm in size (Fig. 3c), sharing straight boundaries with olivine, orthopyroxene, chlorite, and Mag-6; (2) as interstitial grains of up to ~100 μm, occasionally associated with Mag-5 or Mag-6; (3) rare tiny (<10 μm size) inclusions in silicates. Subordinate pyrrhotite is often associated with large subhedral pentlandite, forming indented grain boundaries that cover up to a quarter of the exposed area of the whole grain (Fig. 3c). In the spinifex-textured Chl-harzburgite only interstitial pentlandite and rare pyrrhotite were observed.

Retrograde oxide and sulfide crystallization

Retrogression features are variably prominent in Almirez ultramafic rocks (Fig. 5), particularly in the granular-textured Chl-harzburgite where the extent of retrogression reaches up to 30 vol% of the sample. Retrogression includes formation of talc after orthopyroxene along grain boundaries and cleavage planes (compare fig. 3g of Bretscher *et al.*, 2018; Fig. 5a and b) and crack-filling lizardite and chrysotile (this study; Debret *et al.*, 2015; Fig. 5c and f) with magnetite, both enveloping peak metamorphic minerals and lining typical mesh textures in metamorphic olivine (Fig. 5d). Lizardite also occurs along grain boundaries and cleavages in chlorite.

Opaque minerals are also associated with retrograde hydrous silicates. In the Atg-serpentinite, laths of hematite are found at the rims of Mag-3 in association with yellow serpentine, probably lizardite (Fig. 5e; here too small to be identified by Raman spectroscopy). In the Chl-harzburgite, opaque minerals consist of micrometer-sized magnetite (Mag-7 in Fig. 5d) forming at the interface between prograde olivine and retrograde lizardite, or lining lizardite crack fillings, and hematite exsolutions in ilmenite (and vice versa), very rare pyrite, and chalcopyrite. Moreover, anhedral grains of tiny (<5 μm) chalcopyrite and barite, detected by EDS spectra, were observed in a vermicular hole network in pentlandite.

EPMA major element compositions

Major element composition of oxides and sulfides, and trace element composition of oxides were measured by EPMA and LA-ICP-MS. The medians and the first and third quartiles of oxide minerals compositions (or representative analyses for sulfides) are reported in Tables 2–4; individual measurement data are provided in the Zenodo repository at https://doi.org/10.5281/zenodo.4593408.

Magnetite

Different magnetite populations distinguished on the basis of microtextural position (Figs 2 and 3) are characterized by distinct major element compositions.

In the Atg-serpentinite, magnetite populations are characterized as follows. (1) Anhedral magnetite is zoned (Figs 6 and 7), displaying a core (Mag-1) to rim (Mag-2) decrease in Cr_2O_3 (9·72–5·83 wt%), MgO (2·22–2·02 wt%), TiO_2 (0·74–0·54 wt%), and MnO (1·45–0·80 wt%) along with a slight increase in FeO_{tot} from Mag-1 to Mag-2 (80·6–83·9 wt%). NiO ranges from 0·26 to 0·38 wt%. (2) Matrix Mag-3 has lower Cr_2O_3 (less than 3·61 wt%) and MgO (less than 1·58 wt%), and higher FeO_{tot} (ranging from 87·1 to 92·2 wt%) contents (Fig. 7). $X\mathrm{Fe}^{3+}$ [$X\mathrm{Fe}^{3+} = 100\mathrm{Fe}^{3+}/(\mathrm{Fe}^{3+} + \mathrm{Fe}^{2+})$; 67·1–68·4 %] and NiO (0·22–0·31 wt%) contents are similar to Mag-2. (3) Magnetite inclusions in antigorite in bastite textures (pseudomorph after magmatic orthopyroxene) and mesh textures (pseudomorph after magmatic olivine) are compositionally similar to Mag-2 and Mag-3 (Supplementary Data S1; supplementary data are available for downloading at http://www.petrology.oxfordjournals.org), with average Cr_2O_3, NiO, and MnO contents of 3·12, 0·31, and 0·36 wt%, respectively, indicating equilibration during metamorphism.

In the Chl-harzburgite, magnetite displays a large compositional range (Fig. 7), and Mag-4 records the highest Cr_2O_3 contents measured in all our samples. In the granular-textured Chl-harzburgite, three magnetite populations display distinct ranges in Cr_2O_3 contents, with magnetite inclusion in silicates (Mag-4) being richest in Cr_2O_3 (up to 31·66 wt%), compared with the polygonal aggregates (Mag-5 up to 18·55 wt%; Mag-6 up to 11·37 wt%; Figs 6 and 7; Table 2). A similar trend is observed in Mag-5 from core to rim (Fig. 6b) for MgO (from up to 1·85 wt% down to 0·61 wt%), along with increasing $X\mathrm{Fe}^{3+}$ (from 60·8 to 68·3 %) and FeO_{tot} (72·4–90·3 wt%). The compositions of Mag-5 rims (Fig. 6), closely match those of Mag-6 overgrowths (Fig. 7). Nickel concentrations in different magnetite populations display a large range (0·16–0·65 wt%). In the granular-textured Chl-harzburgite, NiO concentration is

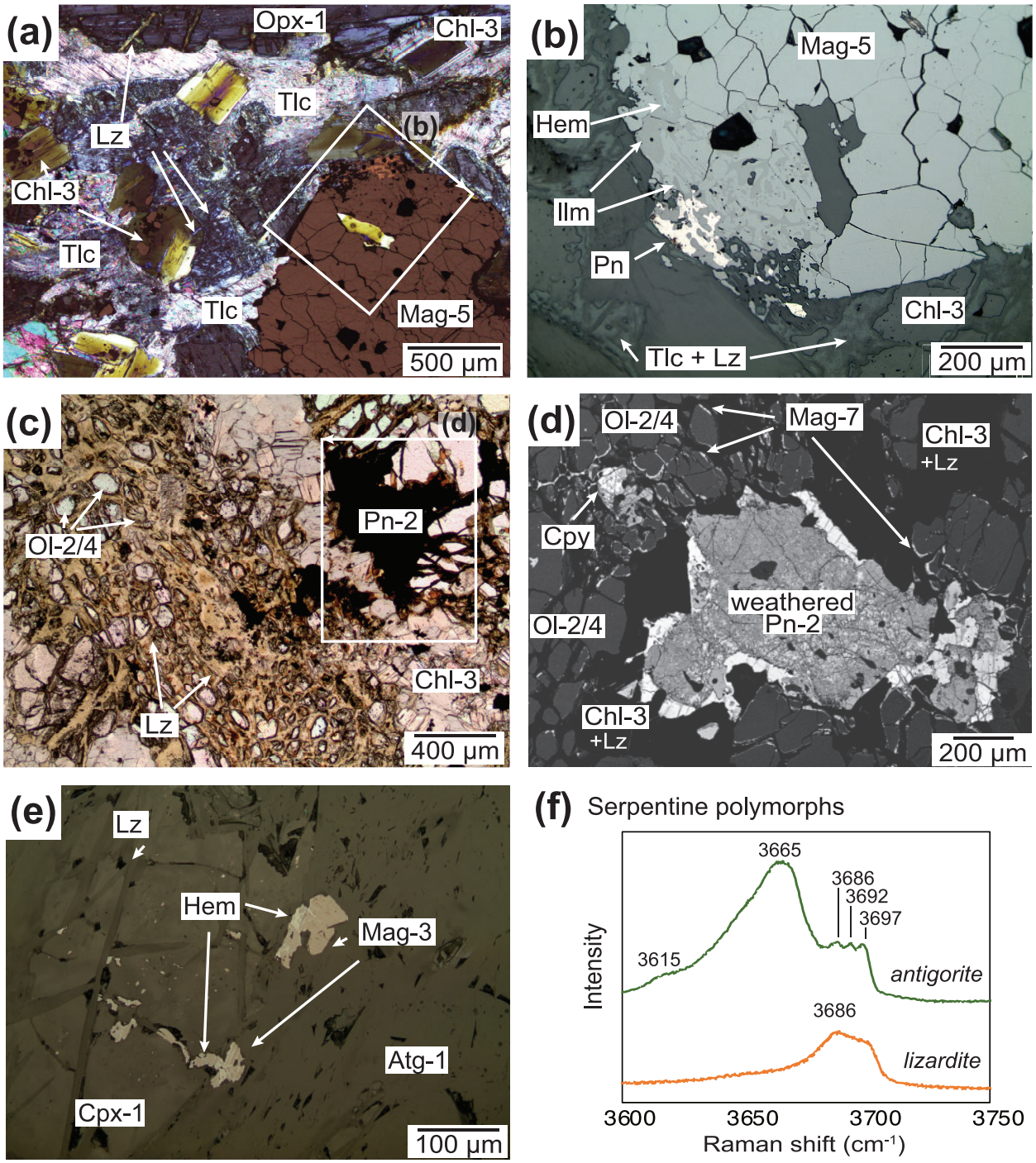

Fig. 5. Retrograde textures affecting mostly the (a–d) Chl-harzburgite and occasionally the (e) Atg-serpentinite [(a) is combined transmitted–reflected light image; (b) and (e) reflected light images; (c) transmitted light image; (d) BSE image]. (a, c) Mesh-type yellow lizardite and talc along crystal boundaries or filling cracks in peak metamorphic olivine, orthopyroxene, and chlorite. (b) Association of magnetite, pentlandite, and exsolved hemo-ilmenite associated with retrograde talc and serpentine. (d) Weathered pentlandite and retrograde crystallization of serpentine and magnetite rims (Mag-7) around peak olivine. (e) Hematite domains in magnetite associated with mesh-type cracks filled with lizardite. (f) Raman spectra of lizardite and antigorite serpentine polysomes as measured in Atg-serpentinite and Chl-harzburgite, respectively, from our sample collection.

on average higher in Mag-4/5 than in Mag-6. Magnetite from spinifex-textured Chl-harzburgite has higher Ni content compared with magnetite from the granular-textured samples, with Mag-4 being the most Ni-rich population, and both Mag-5 and Mag-6 displaying comparable NiO contents (Fig. 7b).

Pentlandite and pyrrhotite

Pentlandite from the Atg-serpentinite and Chl-harzburgite has identical major element composition. Minor variations in Fe, Ni, and Co contents remain within possible stoichiometric variations (Table 3). Pyrrhotite of the granular-textured Chl-harzburgite

Table 2: Median, minimum and maximum element concentrations of each magnetite growth-stage (Mag-1 to Mag-6), obtained by EPMA and LA-ICP-MS

			Atg-serpentinite								
			Mag-1			Mag-2			Mag-3		
			($n=43$)			($n=80$)			($n=52$)		
			median	Q1	Q3	median	Q1	Q3	median	Q1	Q3
EPMA data											
TiO_2			0·58	0·49	0·67	0·34	0·29	0·38	0·19	0·15	0·21
Cr_2O_3			6·52	5·70	7·39	3·77	2·52	4·34	0·64	0·30	2·28
FeO_{tot}			82·61	81·79	84·33	86·96	86·11	88·19	90·41	88·49	91·14
MnO			0·75	0·63	1·11	0·46	0·37	0·55	0·14	0·11	0·32
MgO			1·89	1·77	1·95	1·45	1·35	1·67	0·70	0·62	1·20
Al_2O_3			0·06	0·05	0·07	0·03	0·02	0·04	0·02	0·01	0·03
NiO			0·34	0·32	0·35	0·33	0·31	0·34	0·27	0·25	0·28
LA-ICP-MS data	Mass*	LOD†	($n=14$)			($n=30$)			($n=27$)		
TiO_2	49	0·63	0·46	0·42	0·47	0·31	0·23	0·37	0·21	0·16	0·28
Cr_2O_3	53	1·3	5·85	5·47	6·03	3·58	2·84	3·92	2·50	1·03	3·13
FeO	57	8·5	28·17	27·79	28·38	28·84	28·53	29·01	29·08	28·90	29·19
Fe_2O_3	57	8·5	62·12	61·71	62·29	64·77	64·47	65·66	66·28	65·31	67·63
MnO	55	2·1	0·45	0·42	0·47	0·25	0·21	0·30	0·20	0·16	0·24
MgO	25	0·61	1·65	1·53	1·76	1·21	1·11	1·36	0·98	0·93	1·09
Al_2O_3	27	0·17	0·08	0·06	0·10	0·04	0·02	0·04	0·02	0·01	0·03
NiO	62	0·7	0·29	0·28	0·31	0·29	0·26	0·35	0·26	0·24	0·30
Sc	45	0·07	1·5	1·4	1·5	1·1	0·9	1·2	0·7	0·6	0·8
V	51	0·09	1210	933	1238	763	653	813	728	569	873
Co	59	0·025	174	168	178	158	149	177	116	95	134
Ni	62	0·7	2267	2218	2433	2313	2064	2768	2027	1892	2347
Cu	65	0·07	0·27	0·08	0·6	0·12	0·08	1·4	0·25	0·11	1·8
Zn	66	0·29	566	511	607	278	213	348	197	119	245
Ga	71	0·015	4·3	3·0	4·5	3·3	2·0	3·7	2·8	1·4	3·1
As	75	0·07	0·20	0·13	0·28	0·15	0·10	0·19	0·19	0·08	0·33
Y	89	0·010	0·09	0·05	0·17	0·021	0·013	0·08	0·023	0·015	0·044
Zr	90	0·012	0·16	0·10	0·17	0·05	0·033	0·15	0·034	0·019	0·05
Nb	93	0·007	0·11	0·07	0·14	0·05	0·034	0·08	0·031	0·019	0·036
Mo	95	0·032	0·07	0·07	0·09	0·05	0·042	0·06	0·05	0·033	0·05
Sn	118	0·10	0·37	0·33	0·41	0·24	0·16	0·29	0·18	0·13	0·24
W	182	0·029	0·021	0·021	0·021	0·11	0·06	0·12	0·09	0·05	0·13
Pb	208	0·026	0·044	0·036	0·06	0·05	0·031	0·09	0·05	0·027	0·11
U	238	0·008	0·12	0·06	0·26	0·09	0·043	0·13	0·024	0·008	0·028
XFe^{3+} (calc)‡			0·67	0·67	0·67	0·68	0·68	0·68	0·67	0·67	0·68

			Granular-textured Chl-harzburgite								
			Mag-4			Mag-5			Mag-6		
			($n=57$)			($n=103$)			($n=111$)		
			median	Q1	Q3	median	Q1	Q3	median	Q1	Q3
EPMA data											
TiO_2			0·33	0·18	0·49	0·52	0·38	0·67	0·38	0·37	0·40
Cr_2O_3			4·84	4·03	9·52	8·46	3·68	12·34	2·34	2·27	3·41
FeO_{tot}			85·32	79·79	87·05	83·20	78·56	87·64	88·90	87·82	89·15
MnO			0·72	0·21	1·65	0·21	0·13	0·30	0·42	0·40	0·60
MgO			1·12	0·80	1·71	1·22	0·98	1·46	0·98	0·90	1·04
Al_2O_3			0·14	0·10	0·20	0·24	0·15	0·41	0·14	0·13	0·16
NiO			0·37	0·31	0·49	0·34	0·29	0·39	0·32	0·29	0·35
LA-ICP-MS data	Mass*	LOD†				($n=20$)			($n=20$)		
TiO_2	49	0·63				0·39	0·33	0·51	0·33	0·29	0·49
Cr_2O_3	53	1·3				5·22	3·92	11·83	3·34	2·16	8·92
FeO	57	8·5				29·18	28·95	29·32	29·38	29·23	29·46
Fe_2O_3	57	8·5				62·72	55·50	64·19	64·84	58·78	66·15
MnO	55	2·1				0·10	0·07	0·16	0·07	0·06	0·12
MgO	25	0·61				1·07	0·96	1·27	0·92	0·88	1·01
Al_2O_3	27	0·17				0·16	0·15	0·36	0·13	0·12	0·22
NiO	62	0·7				0·31	0·30	0·32	0·31	0·30	0·35
Sc	45	0·07				10	9	11	9	8	10
V	51	0·09				1605	1368	2469	1408	1305	2019
Co	59	0·025				109	87	141	110	101	137
Ni	62	0·7				2445	2324	2536	2460	2354	2753

(continued)

Table 2: Continued

			Granular-textured Chl-harzburgite								
			Mag-4			Mag-5			Mag-6		
			($n=57$)			($n=103$)			($n=111$)		
			median	Q1	Q3	median	Q1	Q3	median	Q1	Q3
Cu	65	0·07				0·06	0·044	0·09	0·08	0·06	139
Zn	66	0·29				220	144	1405	131	108	780
Ga	71	0·015				7	7	7	7	6	8
As	75	0·07				0·12	0·07	0·22	0·23	0·12	0·42
Y	89	0·010				0·034	0·030	0·05	0·028	0·021	0·11
Zr	90	0·012				0·09	0·06	0·11	0·05	0·039	0·10
Nb	93	0·007				0·06	0·044	0·12	0·05	0·032	0·10
Mo	95	0·032				0·032	0·028	0·039	0·033	0·032	0·042
Sn	118	0·10				1·3	0·6	1·4	1·3	0·6	1·4
W	182	0·029				0·15	0·15	0·15	0·08	0·05	0·10
Pb	208	0·026				0·032	0·032	0·032	0·035	0·030	0·037
U	238	0·008				0·031	0·009	0·10	0·15	0·10	0·25
$X Fe^{3+}$ (calc)‡			0·66	0·66	0·67	0·65	0·64	0·67	0·67	0·67	0·67
			Spinifex-textured Chl-harzburgite								
			Mag-4			Mag-5			Mag-6		
			($n=50$)			($n=18$)			($n=31$)		
			median	Q1	Q3	median	Q1	Q3	median	Q1	Q3
EPMA data											
TiO_2			0·09	0·04	0·24	0·51	0·30	0·55	0·54	0·35	0·59
Cr_2O_3			4·53	0·50	6·48	9·12	6·89	9·60	9·38	6·15	9·93
FeO_{tot}			85·89	82·93	88·65	81·19	80·14	83·07	80·98	79·79	84·98
MnO			0·11	0·07	0·22	0·22	0·16	1·45	0·22	0·12	1·64
MgO			1·04	0·89	1·40	1·54	1·24	1·64	1·35	0·98	1·68
Al_2O_3			0·05	0·02	0·06	0·30	0·17	0·32	0·31	0·16	0·34
NiO			0·51	0·46	0·60	0·53	0·52	0·54	0·53	0·51	0·55
LA-ICP-MS data	Mass*	LOD†				($n=21$)			($n=18$)		
TiO_2	49	0·63				0·47	0·41	0·52	0·44	0·35	0·50
Cr_2O_3	53	1·3				8·26	7·84	9·06	8·35	8·04	8·98
FeO	57	8·5				28·86	28·37	29·32	28·45	28·34	28·52
Fe_2O_3	57	8·5				59·29	58·43	59·66	59·33	58·78	59·94
MnO	55	2·1				0·14	0·12	0·15	0·14	0·13	0·15
MgO	25	0·61				1·35	1·17	1·49	1·40	1·31	1·48
Al_2O_3	27	0·17				0·27	0·23	0·31	0·26	0·24	0·28
NiO	62	0·7				0·52	0·29	0·56	0·56	0·52	0·57
Sc	45	0·07				12	11	13	12	10	13
V	51	0·09				2396	1522	2518	2620	2392	2691
Co	59	0·025				236	99	246	243	236	248
Ni	62	0·7				4060	2308	4386	4367	4067	4476
Cu	65	0·07				0·07	0·07	0·11	0·07	0·06	0·08
Zn	66	0·29				724	647	943	810	670	856
Ga	71	0·015				9	9	12	8	8	9
As	75	0·07				0·08	0·07	0·09	0·14	0·10	0·16
Y	89	0·010				0·025	0·016	0·034	0·030	0·023	0·07
Zr	90	0·012				0·07	0·06	0·09	0·07	0·06	0·08
Nb	93	0·007				0·07	0·07	0·08	0·08	0·07	0·08
Mo	95	0·032				0·037	0·036	0·042	0·034	0·032	0·039
Sn	118	0·10				0·5	0·44	0·5	0·5	0·5	0·6
W	182	0·029				n.a.	n.a.	n.a.	n.a.	n.a.	n.a.
Pb	208	0·026				n.a.	n.a.	n.a.	0·32	0·18	0·46
U	238	0·008				0·05	0·036	0·13	0·026	0·017	0·034
$X Fe^{3+}$ (calc)‡			0·67	0·66	0·68	0·66	0·65	0·66	0·66	0·65	0·66

Element oxide concentrations are expressed in wt% oxide, and element concentrations in $\mu g\,g^{-1}$. Normalization to atoms per formula unit was calculated by stoichiometry. n.a., not analyzed.
*Element mass measured by LA-ICP-MS.
†For measurements with beam size of 30 μm, for all elements expressed as $\mu g\,g^{-1}$.
‡Ratio Fe^{3+}/Fe_{total} was obtained from EPMA data and stoichiometric calculations.

has homogeneous composition with sulfur at 36·9 ± 0·1 wt%, and Fe at 63·6 ± 0·4 wt% (pyrrhotite in the Atg-serpentinite was too small for reliable electron probe measurement).

LA-ICP-MS major to trace element compositions

Magnetite

A suite of lithophile, siderophile, and chalcophile elements (e.g. Mg, Al, Sc, Ti, V, Cr, Mn, Fe, Co, Ni, Zn, Ga, Ge, Y, Zr, Nb, Mo, U, Co, W, Cu, Zn, As, Sn, Sb, and Pb) was measured in magnetite (Table 2; Fig. 8a). A first-order observation is that magnetite trace element patterns largely mirror those of bulk-rock serpentinite formed on the ocean floor (e.g. Kodolányi *et al.*, 2012) and of Atg-serpentinites from Almirez (Fig. 8b). Enrichments in magnetite relative to primitive mantle compositions (PM; Palme & O'Neill, 2014) are observed for U, W, As, Sn, V, Zn, and Cr (Fig. 8b). Trace element

Table 3: Representative EPMA element concentrations for sulfide minerals (pentlandite and pyrrhotite) measured in the Atg-serpentinite and Chl-harzburgite lithologies

	Pentlandite									Pyrrhotite		
	Atg-serp			Chl-harz (granular)			Chl-harz (spinifex)			Chl-harz (granular)		
wt%	1	2	3	4	5	6	7	8	9	10	11	12
S	33·39	22·44	33·28	33·12	33·42	33·33	33·27	33·17	33·21	36·67	36·86	36·82
Fe	30·93	27·51	31·31	29·81	32·25	35·93	33·66	29·12	31·03	63·38	64·57	62·69
Ni	35·32	38·07	34·26	36·2	34·08	29·88	31·78	36·3	33·39	0·04	0·01	0·04
Co	0·42	0·78	1·12	0·84	0·91	0·64	1·44	1·48	2·51	0·1	0·07	0·09
Cu	<0·01	<0·01	<0·01	<0·01	<0·01	<0·01	<0·01	<0·01	<0·01	<0·01	<0·01	<0·01
Zn	<0·01	0·02	<0·01	<0·01	<0·01	<0·01	<0·01	0·01	<0·01	<0·01	0·01	0·02
Pb	0·12	0·17	0·04	0·05	0·1	0·21	<0·01	<0·01	<0·01	0·06	<0·01	0·17
Total	100·17	99·99	100·01	100·02	100·76	99·99	100·15	100·08	100·14	100·26	100·52	99·83

Table 4: LA-ICP-MS data expressed as median and first and third quartiles of chemical concentrations (μg g^{-1}) of wormy ilmenite and hemo-ilmenite grains from granular-textured Chl-harzburgites, and ilmenite rims and ilmeno-hematite grain-types from spinifex-textured Chl-harzburgite

		Granular-textured Chl-harzburgite				Spinifex-textured Chl-harzburgite					
		Wormy Ilm.	Hemo-ilmenite			Ilmenite rims			Ilmeno-hematite		
		(*n* = 1)	(*n* = 10)			(*n* = 3)			(*n* = 8)		
		median	median	Q1	Q3	median	Q1	Q3	median	Q1	Q3
Oxide (wt%)											
TiO_2		50·68	43·89	43·12	44·40	52·05	50·52	52·05	17·93	17·05	18·95
Cr_2O_3		0·20	1·10	0·81	1·16	0·20	0·18	0·24	3·20	3·09	3·30
FeO		35·90	30·18	29·49	30·85	34·71	33·70	34·83	13·23	12·37	13·65
Fe_2O_3		6·54	18·65	17·76	19·45	5·14	5·07	7·92	61·94	60·48	63·92
MnO		1·40	0·55	0·53	0·56	0·69	0·68	0·69	0·16	0·14	0·16
MgO		4·67	4·86	4·74	4·99	6·31	6·20	6·38	2·08	1·95	2·30
Element (μg g^{-1})	Mass										
Al	27	48	46	43	61	65	63	72	260	244	272
Sc	45	289	224	216	233	315	312	326	181	173	192
V	51	381	1090	883	1162	530	523	630	3164	3006	3269
Co	59	45	58	48	66	87	83	88	61	56	65
Ni	62	207	371	234	442	353	343	365	353	338	382
Cu	65	4·1	3·4	2·4	4·4	4·1	4·0	4·2	1·5	1·1	1·9
Zn	66	187	110	107	118	212	212	227	36	33	40
Ga	71	0·26	0·26	0·24	0·30	0·23	0·21	0·28	1·1	1·0	1·3
As	75	0·27	0·24	0·16	0·30	0·39	0·35	0·43	0·39	0·33	0·5
Y	89	0·30	0·28	0·22	0·34	0·14	0·10	0·16	0·29	0·21	0·34
Zr	90	17	14	12	14	16	16	17	15	13	16
Nb	93	272	271	249	278	436	418	438	13	9	16
Mo	95	0·16	0·14	0·13	0·18	0·21	0·21	0·21	0·19	0·17	0·20
Sn	118	28	6	6	7	13	12	16	16	13	17
W	182	0·11	0·07	0·05	0·11	0·29	0·26	1·01	0·044	0·044	0·044
Pb	208	<0·07	0·19	0·15	0·23	0·7	0·7	0·7	0·14	0·14	0·14
U	238	0·8	0·28	0·24	0·36	0·12	0·11	0·12	0·15	0·12	0·18
XFe^{3+}(calc)*		0·14	0·36	0·34	0·37	0·12	0·12	0·17	0·81	0·80	0·82
V/Sc		1·3	4·5	3·9	5·1	1·7	1·6	2·0	17·3	16·6	18·0
Nb/Sc		0·94	1·20	0·94	1·28	1·30	1·28	1·36	0·07	0·05	0·08

It should be noted that the ilmenite rim around ilmeno-hematite grains (compare Fig. 10b) is not incorporated in the sample volume measured by LA-ICP-MS.

*Ferric to total iron ratio (XFe^{3+}) was calculated by stoichiometry, considering a structural formula of three oxygens and two cations.

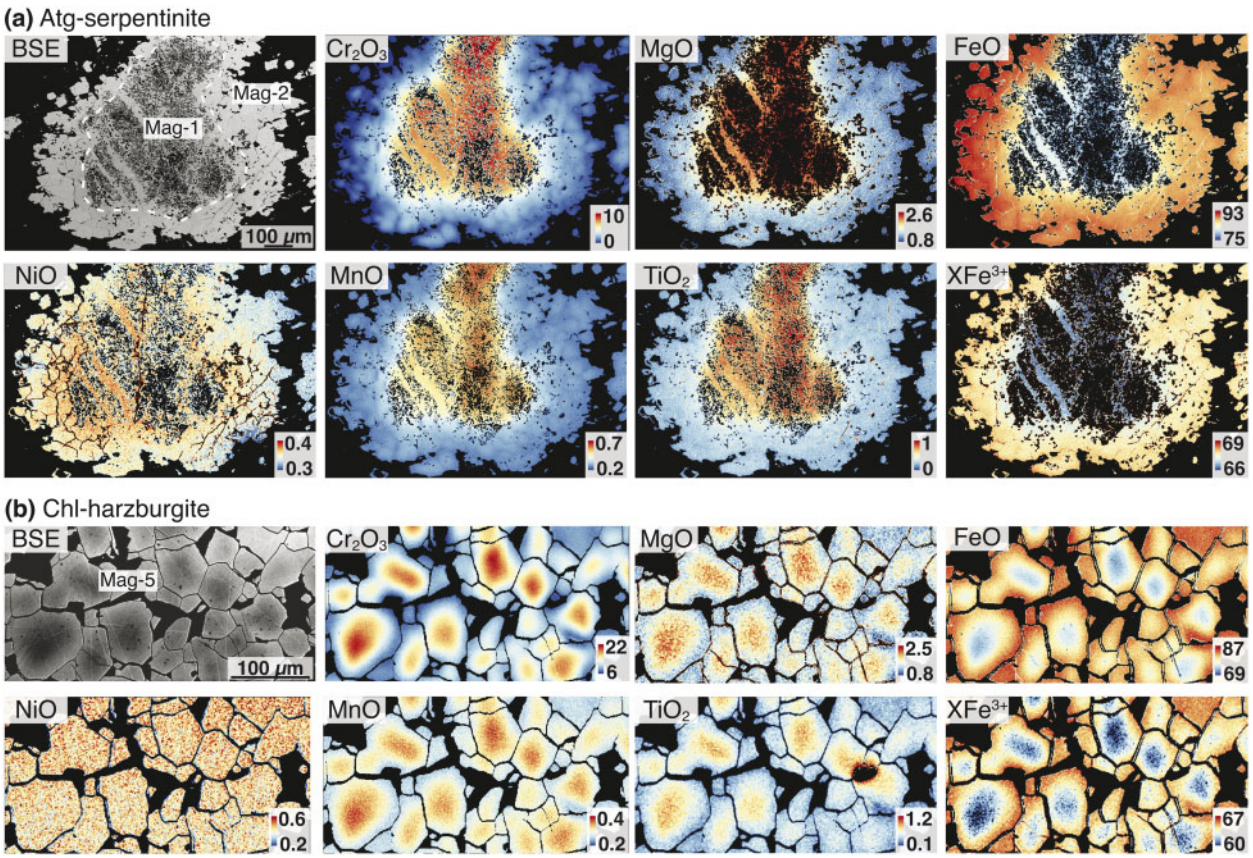

Fig. 6. EPMA elemental maps of (a) Mag-1 and Mag-2 from Atg-serpentinite and (b) Mag-5 from the granular Chl-harzburgite. For each image, a color-coded bar indicates the concentration in weight per cent, except for $X\mathrm{Fe}^{3+}$, which indicates the molar ratio $\mathrm{Fe}^{3+}/(\mathrm{Fe}^{2+} + \mathrm{Fe}^{3+})$.

concentrations in magnetite from Atg-serpentinite and Chl-harzburgite largely overlap (Figs 7 and 8). Intra-sample variability for magnetite in the Atg-serpentinite and Chl-harzburgite can exceed potential differences between the two rock-types (Table 2). Nevertheless, some key elements such as Cr, V, Zn and Mn show significant variability among rock-type and magnetite populations (Fig. 9).

Magnetite in the Atg-serpentinite (large anhedral crystals Mag-1 and Mag-2) shows overall decreasing trace element concentrations from core (Mag-1) to rim (Mag-2), mimicking major element systematics (compare compositional maps in Fig. 6). Aluminum ranges from $\sim$420 $\mu g\,g^{-1}$ (Mag-1) to $\sim$190 $\mu g\,g^{-1}$ (Mag-2; Fig. 9a), V from $\sim$1200 to $\sim$760 $\mu g\,g^{-1}$ (Fig. 9b), and Zn from $\sim$570 to $\sim$280 $\mu g\,g^{-1}$ (Fig. 9c), showing similar trends also for Co, Ga (4·3–3·3 $\mu g\,g^{-1}$), Sc (1·5–1·1 $\mu g\,g^{-1}$), Y, and U (0·12–0·09 $\mu g\,g^{-1}$). In contrast, chalcophile element concentrations are fairly constant from Mag-1 to Mag-2; for example, As $\sim$0·20 $\mu g\,g^{-1}$, Cu $\sim$0·27 $\mu g\,g^{-1}$, and Pb $\sim$0·044 $\mu g\,g^{-1}$. Matrix Mag-3 is compositionally very close in both major and trace elements to Mag-2 (see Table 2).

Magnetite in the Chl-harzburgite shows uniform trace element composition across Mag-5 to Mag-6 populations (Mag-4 was too small to be measured by LA-ICP-MS). Magnetite in the spinifex-textured Chl-harzburgite shows higher trace element concentrations relative to the granular-textured ones, and enrichment trends correlate well with major elements (e.g. Al vs Cr; Fig. 9a). Core to rim zonation observed in the polygonal Mag-5 (compare Fig. 6), shows a decrease in Cr, from as high as 110 000 $\mu g\,g^{-1}$ in the core to 9700 $\mu g\,g^{-1}$ in the rim. Figure 9 shows the correlation of Cr decrease with decreasing elemental trends in Al (2400–600 $\mu g\,g^{-1}$), V (2800–1300 $\mu g\,g^{-1}$), Zn (2000–70 $\mu g\,g^{-1}$), and Mn (2000–350 $\mu g\,g^{-1}$). As observed for major elements, trace element concentrations of Mag-5 rims and Mag-6 are very similar.

Ilmenite and hemo-ilmenite/ilmeno-hematite

Major and trace element concentrations of ilmenite and the ilmenite–hematite solid solution minerals were measured by LA-ICP-MS (Fig. 10a; Table 4). A large beam size (38–50 μm) was employed for LA-ICP-MS measurement of exsolved hemo-ilmenite and ilmeno-hematite domains to determine the respective pre-exsolution single-phase compositions, as illustrated in the insets of Fig. 10b. Hemo-ilmenite and ilmeno-hematite solid solution compositions are governed by the substitution $\mathrm{Ti}^{4+} + \mathrm{Fe}^{2+} = 2\mathrm{Fe}^{3+}$, and measured pre-exsolution compositions range from 0·83Ilm/0·17Hem to 0·30Ilm/0·70Hem (Fig. 10b). Higher ilmenite

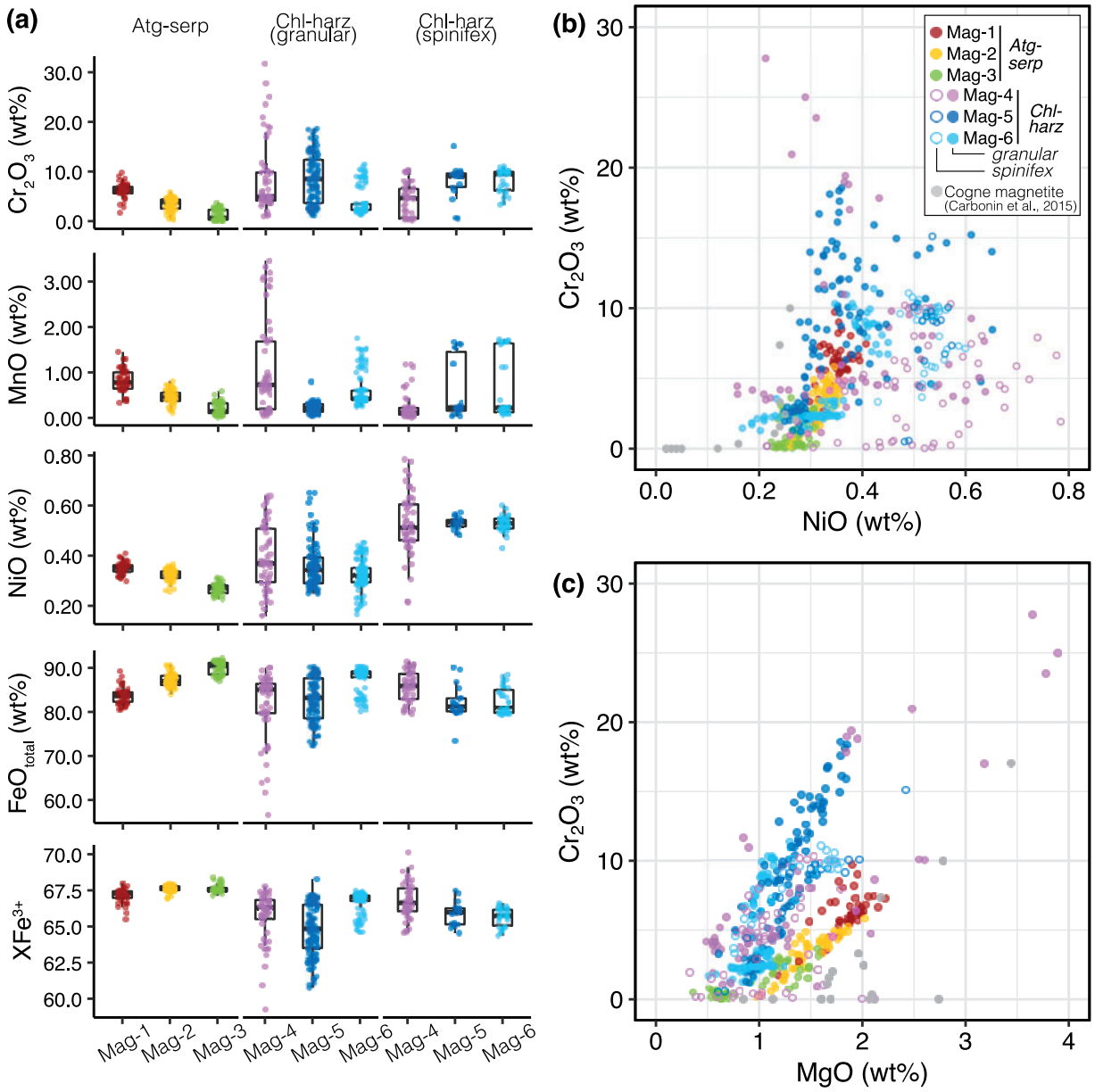

Fig. 7. Major element chemistry of magnetite obtained by EPMA for successive magnetite crystallization stages with the legend displayed in (b). (a) Boxplot over the colored spots representing individual measurement data with median, 1st and 3rd quartile of Cr_2O_3, MnO, NiO, total FeO, and XFe^{3+} concentrations in magnetite. (b, c) Elemental plots showing variations in Cr_2O_3 with NiO and MgO. $XFe^{3+} = 100Fe^{3+}/(Fe^{3+} + Fe^{2+})$ molar. Magnetite compositions from the orogenic serpentinite-hosted Cogne hydrothermal deposit (Carbonin *et al.*, 2015) are plotted in grey for comparison.

components are, however, found in wormy ilmenite in granular-textured Chl-harzburgite and in ilmenite rims around ilmeno-hematite in spinifex-textured Chl-harzburgite (0·90Ilm/0·10Hem to 0·95Ilm/0·05Hem).

Notable enrichments in U (0·28–0·15 $\mu g\,g^{-1}$), Y (0·28–0·29 $\mu g\,g^{-1}$), Zr (14–15 $\mu g\,g^{-1}$), W (0·07–0·044 $\mu g\,g^{-1}$), Sc (220–180 $\mu g\,g^{-1}$), Nb (270–13 $\mu g\,g^{-1}$), Mo (0·15–0·19 $\mu g\,g^{-1}$), Sn (6–16 $\mu g\,g^{-1}$), and Ti (26·0–11·0 wt%) are observed, respectively, from hemo-ilmenite to ilmeno-hematite relative to magnetite compositions (see PM-normalized concentrations in Fig. 10a). Gallium, Zn, Co, and Ni are depleted relative to magnetite. Niobium is most enriched in hemo-ilmenite relative to PM (Fig. 10a), whereas Cr concentrations are only slightly above PM and Ni slightly below. Hemo-ilmenite solid solution and ilmenite rims display Nb/Sc ratios of 0·7–1·5 that are closely comparable with Ti-clinohumite (Ti-Chu) compositions from the same lithologies [Ti-Chu data from Bretscher (2017)], along with variable V/Sc ratios (1·3–6·0). These are different from ilmeno-hematite grains, which display lower Nb/Sc (0·03–0·10) along with higher V/Sc ratios (13–21). The Nb/Sc ratios in magnetite overlap with the hemo-ilmenite types, whereas V/Sc ratios are higher (Fig. 10c).

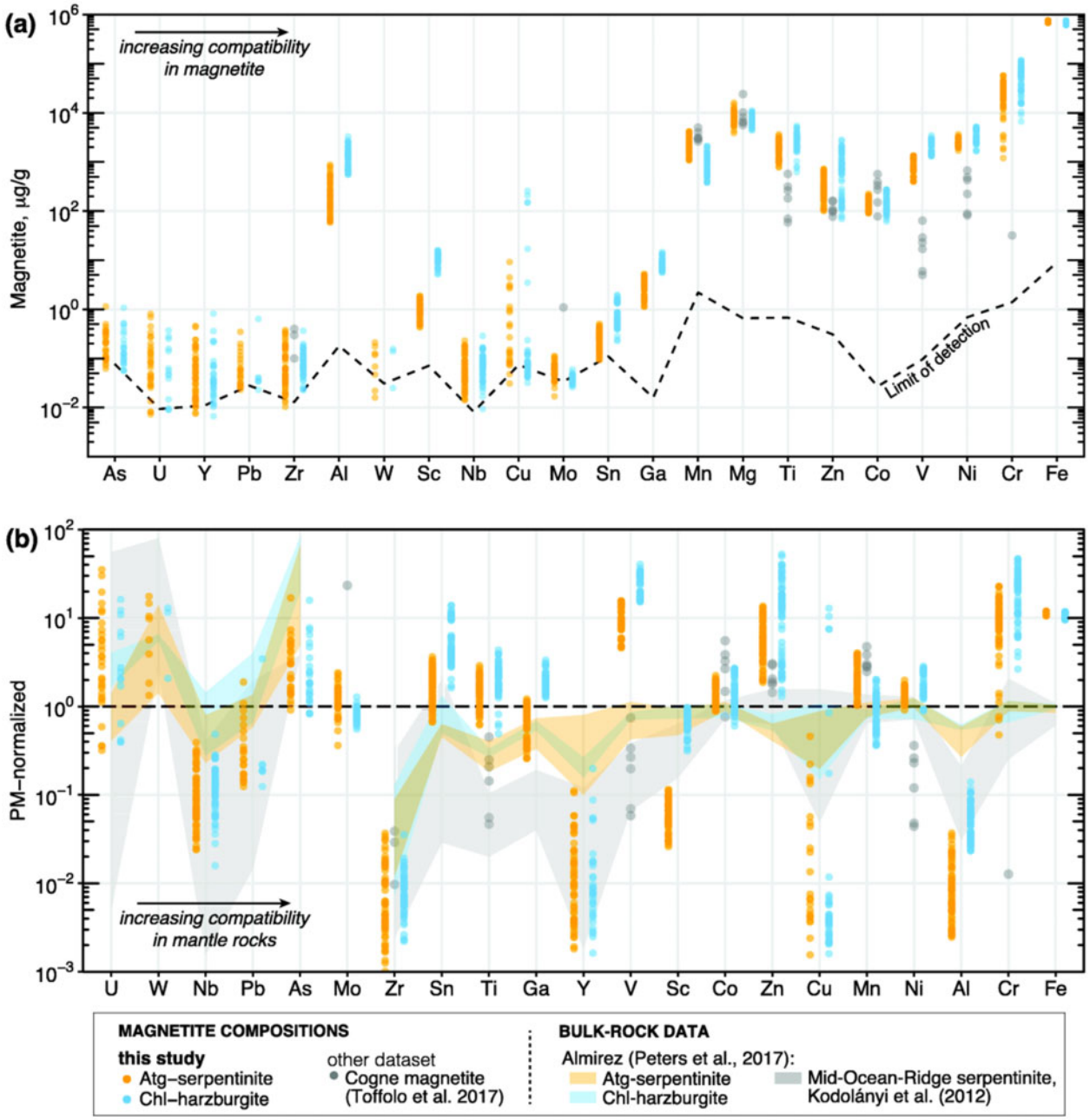

Fig. 8. Major to trace element chemistry of magnetite obtained by LA-ICP-MS. Data from the present study for Cerro del Almirez appear as colored symbols and areas, and data from other localities are reported in grey for comparison. (a) Elemental concentrations of magnetite ordered by increasing compatibility in magnetite of magmatic and hydrothermal origin (after Dare *et al.*, 2012). The black dashed line represents measurement LODs achieved for a 30 µm laser beam size. (b) Primitive mantle (PM; Palme & O'Neill, 2014) normalized major to trace element chemistry of magnetite, compared with bulk-rock data from slow-spreading mid-ocean ridge serpentinite (Kodolányi *et al.*, 2012) and Almirez Atg-serpentinite and Chl-harzburgite (Peters *et al.*, 2017). Element order on the *x*-axis follows the element compatibility trend in mantle rocks. Magnetite concentrations in the Atg-serpentinite (orange symbols) and Chl-harzburgite (blue symbols) are from the present study, compared with magnetite from the serpentinite-hosted Cogne hydrothermal deposit (grey symbols; Toffolo *et al.*, 2017).

Element distribution between rock-forming minerals

Comparison of modeled bulk-rock compositions based on abundance-weighted element concentrations of the peak rock-forming minerals with measured bulk-rock compositions for the Atg-serpentinite and Chl-harzburgite allows identification of the main host minerals for a given element and assessment of the effect of retrogression on bulk-rock compositions (Fig. 11). The modeled bulk was obtained using mineral composition, volume abundance and density following the procedure of Lanari & Engi (2017; further details on the method are given in Supplementary Data S2). Modeled bulk-rock compositions include antigorite,

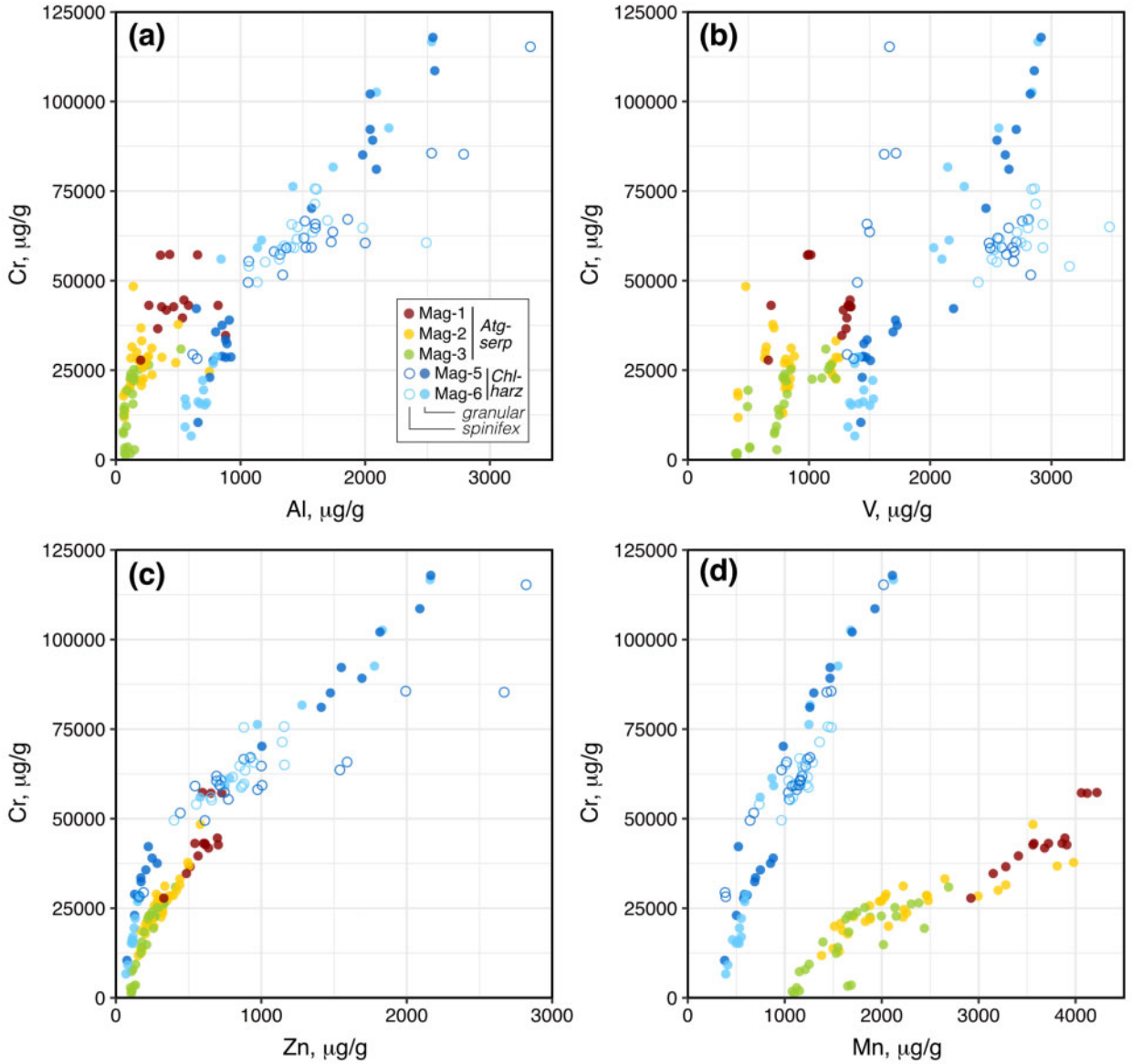

Fig. 9. Elemental plots of Cr versus selected trace elements of magnetite growth-stages, as specified in the legend in (a), obtained by LA-ICP-MS.

olivine, chlorite, tremolite, orthopyroxene, magnetite, and pentlandite. Ti-clinohumite and ilmenite–hematite solid solution minerals were not considered because their modes are significantly below 1%. Clinopyroxene was also excluded, because its modes are low in the Atg-serpentinite and it is absent in the Chl-harzburgite. Results are displayed in Fig. 11 (and summarized in Table S2.4 of Supplementary Materials), where modeled bulk compositions are normalized to measured bulk-rock compositions for which measured Fe^{2+} and Fe^{3+} concentrations are available (Padrón-Navarta *et al.*, 2011).

For the Atg-serpentinite (Fig. 11a), modeled and measured bulk compositions agree to within 15%, for most of the element ratios (modeled bulk/measured bulk) close to unity. For the Chl-harzburgite (Fig. 11b, c), modeled versus measured Si, Mg, Mn, Ni, Fe_{tot}, ±Cr, and ±Al bulk contents agree to within 25% irrespective of texture. However, despite the good match for Fe_{tot} (modeled bulk/measured bulk is 1·12 in the Atg-serpentinite, and 1·07 and 1·13, respectively, in the spinifex- and granular-textured Chl-harzburgite), the Fe^{3+}:Fe^{2+} proportion is significantly different between modeled and measured bulk, Fe^{3+} being *c.* 40% higher in the measured bulk-rock sample. The higher proportion of Fe^{3+} in bulk-rock measurements can plausibly be explained by the presence of retrograde lizardite along with minor magnetite and hematite laths, notably in the Chl-harzburgite (see above; Fig. 2).

In serpentinite bulk-rock, antigorite is an important carrier for all the elements considered, whereas magnetite is the dominant host for Fe^{2+} and Fe^{3+}, and is relevant for Cr and V. Figure 11 also illustrates the element partitioning between the reaction products olivine, chlorite, and

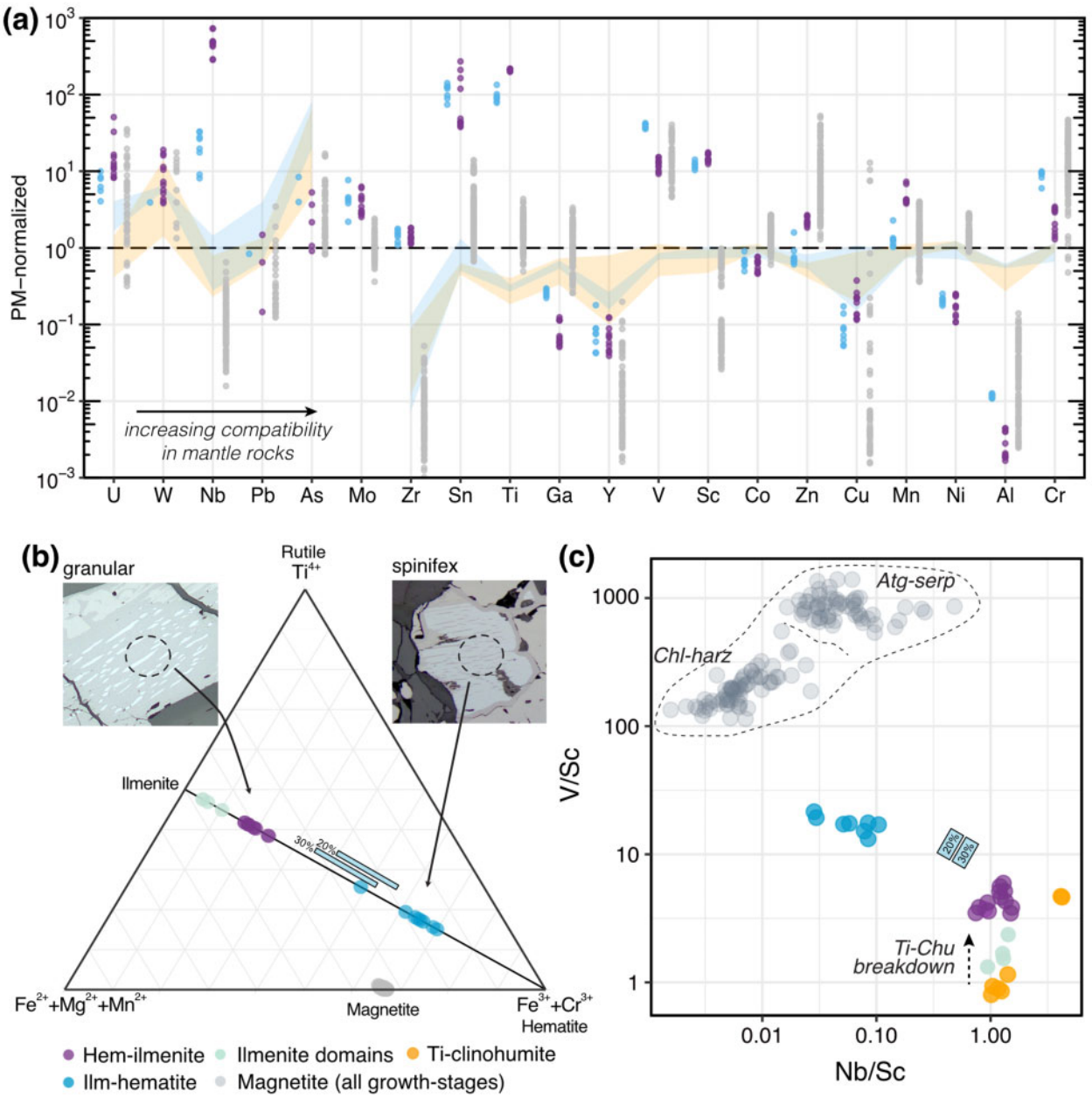

Fig. 10. Major to trace element chemistry of the textural types of the ilmenite–hematite solid solutions obtained by LA-ICP-MS. (a) Element concentrations of each mineral type [legend is shown in (b)] normalized to primitive mantle (PM; Palme & O'Neill, 2014). PM-normalized bulk-rock data for Almirez Atg-serpentinite and Chl-harzburgite (Peters *et al.*, 2017) are plotted as yellow and blue areas for comparison, respectively. (b) Pre-exsolution ilmenite–hematite compositions on the ternary $(Fe^{2+} + Mg^{2+} + Mn^{2+})$–$(Fe^{3+} + Cr^{3+})$–$Ti^{4+}$ diagram, expressed in atoms per formula unit based on LA-ICP-MS measurements. Microphotograph insets show an example of the sampling spot size employed for exsolved Hem–Ilm and Ilm–Hem, in the granular- and spinifex-textured Chl-harzburgites (grains about 100 μm). (c) Plot of Nb/Sc vs V/Sc. Titanium-clinohumite data (from Bretscher, 2017) and magnetite compositions (Mag-1 to Mag-6; present study) are added for comparison. In (b) and (c) rectangles are displayed for reintegrated ilmenohematite compositions including the 20 % and 30 % ilmenite rim.

orthopyroxene. Chlorite is the prime host for Al along with prominent Cr, V, and Fe^{3+}. Olivine and orthopyroxene host most Si, Mg, Mn, and Fe^{2+}, and Ni. Pentlandite together with antigorite, or olivine, hosts most of the Ni.

DISCUSSION

Magnetite along with subordinate ilmenite, ilmenite–hematite solid solutions, pentlandite, and pyrrhotite are stable in the investigated samples throughout the entire subduction–exhumation metamorphic cycle. Figure 12 summarizes the main textural and geochemical features of magnetite in the Atg-serpentinite and Chl-harzburgite. The stability of the above-mentioned opaque minerals and their role in metamorphic reactions with progressive subduction, as monitored by compositional characteristics, is discussed with focus on the antigorite-breakdown reaction. In a first stage, the

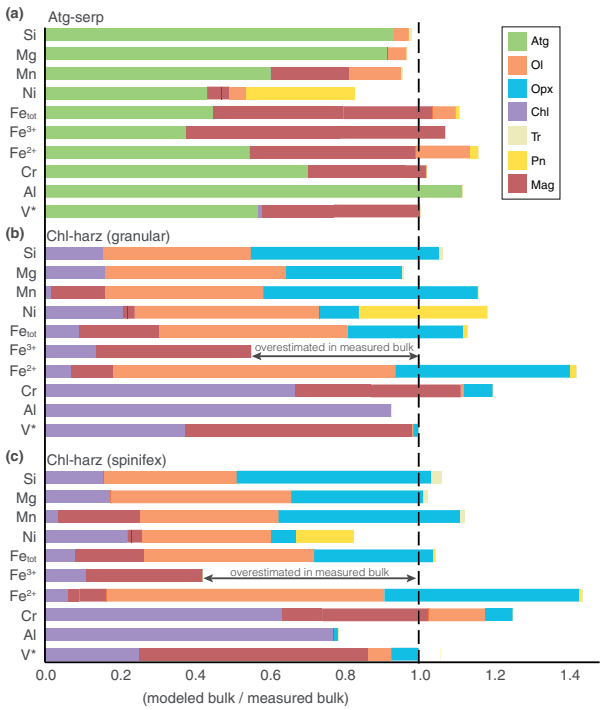

Fig. 11. Element distribution diagrams for the prograde rock-forming minerals of (a) Atg-serpentinite, and (b) granular-textured and (c) spinifex-textured Chl-harzburgite. Diagrams compare the modeled bulk compositions with a measured bulk-rock composition. Values below the 1·0 line represent underestimation of the modeled bulk when compared with measured bulk and vice versa for values above the 1·0 line. This diagram illustrates how severely bulk-rock measurements can overestimate peak-metamorphic Fe^{3+} contents, owing to inclusion of Fe^{3+} formed upon rock retrogression. Vanadium* was normalized to unity because there are no bulk-rock data available for V. Details of the model calculations are presented in Supplementary Data S2.

importance of recognizing and distinguishing retrograde from prograde mineral growth is addressed, emphasizing how strongly biased bulk-rock data can be if such retrogression is not accounted for. Second, it is discussed how magnetite compositions evolve with prograde mineral reactions, starting with the oceanic to early metamorphic stage recorded in the Atg-serpentinites, followed by evidence for recrystallization and formation of new magnetite across the antigorite-dehydration reaction. Finally, the stability and formation mechanisms of trace occurrence of ilmenite–hematite solid solution minerals is also addressed, and the relevance of exsolved hematite formed during retrogression. This all aims at constraining the rock-buffered fO_2 prevailing during and after antigorite dehydration, to estimate how much redox budget could be transported away in the liberated dehydration fluid.

Importance of recognizing rock retrogression features

Retrogression of peak metamorphic assemblages formed talc, low-temperature lizardite and chrysotile, along with magnetite and trace hematite, pyrite, chalcopyrite, barite, and apatite (see Fig. 5). These texturally late minerals are present in veinlets cutting across peak metamorphic mineral assemblages or replace these inwards from grain boundaries and cracks. Retrogression is much more prominent in massive Chl-harzburgite than in schistose Atg-serpentinites. Previous studies have reported the presence of retrogression (e.g. Padrón-Navarta *et al.*, 2011; Debret *et al.*, 2015) that can form up to ~30 vol% (Bretscher *et al.*, 2018, this study).

The excess of Fe^{3+} for measured relative to calculated bulk-rock compositions reported here (Fig. 11) can be explained by the presence of retrograde serpentine and fine-grained magnetite and hematite. This hypothesis is supported by measured loss on ignition (LOI) values, which range from 4·0 to 6·6 wt% (Padrón-Navarta *et al.*, 2011; Peters *et al.*, 2017). The modes of peak metamorphic chlorite are fixed by bulk-rock Al_2O_3. Considering the composition of rocks in this study, chlorite can account for only 1·5–3 wt% bulk-rock LOI. Therefore, the measured LOI includes retrograde talc and serpentine. In addition, considering $X\mathrm{Fe}^{3+}$ ~0·8 for retrograde chrysotile (Debret *et al.*, 2015), the missing Fe^{3+} in Fig. 11b and c can be compensated for by addition of ~25 vol% chrysotile and some late oxides. Late retrogression and rehydration upon exhumation thus can cause significant oxidation and sulfide (re-)crystallization.

Our results highlight how implications for the redox state of subducting ultramafic rocks based on bulk-rock data can be biased. *In situ* mineral data on prograde to peak metamorphic mineral assemblages are essential to better constrain the oxidizing capacity of dehydrating serpentinites. Moreover, constraints on fO_2 prevailing during peak metamorphic conditions need to be derived from the homogeneous ilmenite–hematite solid solution minerals and not on the basis of the mere presence of exsolved hematite, which we interpret to have formed during cooling and exhumation (as discussed below).

Assessing magnetite stability from geochemistry

Ocean-floor stage preserved in the Atg-serpentinite

Petrographic and chemical signatures recorded in Mag-1 to Mag-2/3 in the Atg-serpentinites document prograde to peak mineral reactions starting upon oceanic serpentinization. This includes the formation of Cr-bearing magnetite after Cr-spinel during ocean-floor serpentinization, and the (re-)crystallization of magnetite in the presence of stable sulfide during subduction.

Oceanic mantle rock hydration involves the formation of serpentine minerals (± brucite) and increasing modes of magnetite (Mag-1–2–3) crystallization with progressive peridotite hydration (e.g. Andreani *et al.*, 2013) at temperatures below 350 °C (Agrinier & Cannat, 1997). No spinel relic was found in Mag-1, but the high Mag-1 Cr_2O_3 contents (up to 14 wt%) suggest ocean-

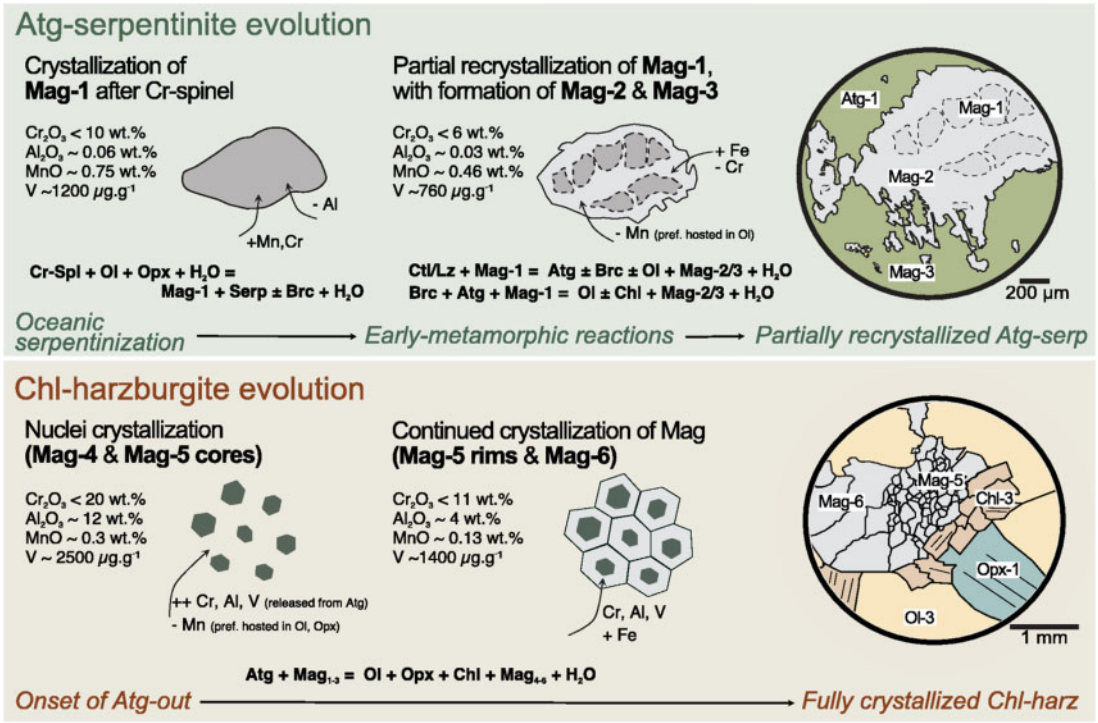

Fig. 12. Sketch illustrating the successive magnetite crystallization stages and their Fe, Cr, Al, Mn and V element inventory, summarizing how magnetite compositions at Almirez evolve with progressive subduction metamorphism to beyond antigorite-out reaction.

floor crystallization at the expense of mantle Cr-spinel along with partial oxidation (Evans & Frost, 1975).

In a second stage, metamorphic magnetite (re-)crystallization formed inclusion-free Mag-2 rims around Mag-1, and Mag-3 displaying equilibrium textures with antigorite. The exact timing of prograde Mag-2 and Mag-3 (re-)crystallization is difficult to assess. However, uniform compositions of magnetite tracing bastite after orthopyroxene, and mesh textures after olivine, in matrix Mag-3 strongly suggest chemical resetting of the oceanic signatures (Supplementary Data S1). Moreover, these magnetite compositions are indistinguishable from Mag-2 recrystallization rims on Mag-1 that formed after spinel on the ocean floor (Fig. 3). Therefore, their lower Cr (0·05–6·34 wt% Cr_2O_3), Mg, Mn, Ni, Ti, Zn, and V, and slightly higher Fe (Figs 7 and 9) most probably result from element redistribution during metamorphic reactions involving silicate minerals and being possibly related to an increase in modal magnetite. Two possibilities can be considered. One is the prograde transformation of lizardite into antigorite starting at ~300 °C (Schwartz *et al.*, 2013), which is accompanied by a decrease of Fe^{3+} in the serpentine mineral that can promote the formation of magnetite (Evans *et al.*, 2012), according to the extended reaction [proposed by Evans (2004)] in equation (1):

$$\mathrm{Ctl/Lz} + \mathrm{Mag-1} = \mathrm{Atg} \pm \mathrm{Brc} \pm \mathrm{Ol} + \mathrm{Mag-2/3} + \mathrm{H_2O}. \quad (1)$$

Another possibility is the brucite-breakdown reaction (Evans & Trommsdorff, 1970) that involves the formation of olivine ± chlorite, as described in equation (2):

$$\mathrm{Brc} + \mathrm{Atg} + \mathrm{Mag-1} = \mathrm{Ol} \pm \mathrm{Chl} + \mathrm{Mag-2/3} + \mathrm{H_2O}. \quad (2)$$

With olivine and chlorite formation, Mn and Al will be preferentially hosted in the silicate phases, consequently reducing their availability for incorporation into magnetite, which, assisted by the presence of aqueous fluid, partially recrystallizes. Moreover, the decrease in Mag-2/3 Cr concentration relative to Mag-1 is best explained by recrystallization and formation of new magnetite, incorporating ferric iron that was hosted in lizardite [equation (1)] or antigorite [equation (2)]. A similar process is also suggested by prominent magnetite crystallization in brucite-dehydration veins present in many Atg-serpentinites from other localities (e.g. Erro Tobio: Scambelluri *et al.*, 1991; 2001; Peters *et al.*, 2020; Zermatt: Kempf *et al.*, 2020). In addition, the decreasing Ni content observed from Mag-1 to Mag-2/3 could also indicate that (re-)crystallization of magnetite occurred in the presence of stable sulfide (i.e. pentlandite), as documented in Fig. 3, and new metamorphic olivine. Comparison of Mag-1 to Mag-3 with available literature data of serpentinite-hosted hydrothermal magnetite from Cogne, Western Alps (Carbonin *et al.*, 2015; Toffolo *et al.*, 2017), shows generally higher Mn and Mg, and lower Zn, V, Ni and Cr concentrations (Figs 7 and 8). Compared with our data, the

geochemical signatures of Cogne magnetite indicate a more intense seafloor alteration stage and a lower metamorphic grade experienced during the Alpine orogeny.

Recrystallization and neo-formation of magnetite across antigorite-out reaction

In the Chl-harzburgite, magnetite shows distinct textures (i.e. forming characteristic inclusion-free polygonal aggregates Mag-5; Fig. 3) and larger compositional ranges compared with magnetite in the Atg-serpentinite (Figs 7–9). Inclusions of Mag-4 in product silicates of the antigorite-breakdown reaction (i.e. olivine, orthopyroxene, and chlorite) represent the oldest textural type of magnetite in the Chl-harzburgite. Mag-4 is characterized by much higher trace element concentrations (including Cr, Al, V, and Zn) relative to Mag-1 and Mag-2/3 of the Atg-serpentinite (Table 3), and closely resembles core compositions of polygonal Mag-5 (Fig. 5; Table 2). Higher Al contents of Mag-4 to Mag-6 compared with Mag-2/3 provide evidence for high-temperature (Evans & Frost, 1975), fluid-assisted complete recrystallization of precursor magnetite (Mag-1 to Mag-3) and/or new magnetite growth according to a generalized reaction involving also oxides and sulfides:

$$\mathrm{Atg} + \mathrm{Mag{-}1/2/3} + \mathrm{sulfide_1} = \mathrm{Ol} + \mathrm{Opx} + \mathrm{Chl} + \mathrm{Mag{-}4/5/6} + \mathrm{sulfide_2} + \mathrm{H_2O}. \quad (3)$$

Antigorite is the major silicate host of Cr, Al, Zn, V, Sc, As, and U in the Atg-serpentinite (Bretscher, 2017; Peters *et al.*, 2020), and is particularly relevant for Cr, Fe, Al, and V in bulk-rock Atg-serpentinite (Fig. 11; Supplementary Data S3). Upon complete antigorite breakdown, these elements are redistributed among the reaction products, including magnetite. This approach has been applied to silicates (e.g. olivine; Scambelluri *et al.*, 2014), but never involving magnetite. Manganese is a good example to illustrate this redistribution. As antigorite has a low affinity for Mn, the coexisting magnetite is rich in Mn. After the antigorite breakdown, newly formed olivine and orthopyroxene have a high affinity for Mn and, as a consequence, Mag-5 and Mag-6 plot overall at lower Mn concentrations than Mag-2/3. The distinct trends in the Cr vs Mn plot (Fig. 9d) reflect the low amounts of olivine coexisting with magnetite in the Atg-serpentinite and the high amounts of olivine + orthopyroxene coexisting with magnetite in the Chl-harzburgite, in full agreement with oxide modes (Table 1). However, the systematics is somewhat complicated by the fact that Mn contents also depend on the amount of magnetite present in the assemblage. An alternative approach based on Cr–V–Al–Fe^{3+} mass balance is presented below to address magnetite production or consumption across the antigorite dehydration.

Significance of ilmenite–hematite solid solution minerals in the Chl-harzburgites

In the Atg-serpentinite, ilmenite–hematite solid solution minerals are rare (<1 vol% of total oxides) and of very small grain size, whereas in the Chl-harzburgites they are slightly more abundant (~4 vol% of total oxides) and have a grain size large enough for LA-ICP-MS measurements. For this reason, the following discussion focuses on the Chl-harzburgites.

The typical oxide assemblage present in the Chl-harzburgites is magnetite + hemo-ilmenite (0·81Ilm/0·19Hem) in granular-textured samples, or magnetite + ilmeno-hematite (0·36Ilm/0·64Hem) with ilmenite mantles in the spinifex-textured samples. Textures suggest that both ilmenite–hematite solid solution minerals formed in equilibrium with the peak mineral assemblage (i.e. olivine, orthopyroxene, chlorite, magnetite; Fig. 4) at ~670 °C; that is, above the ilmenite–hematite solvus temperature of ~600 °C (Ghiorso, 1990; Frost, 1991). The exsolution textures of these grains (Figs 4c, d and 10b) are therefore attributed to formation upon cooling, when the homogeneous minerals enter the solvus. Consequently, only the bulk composition of ilmenite–hematite solid solution minerals is relevant to constrain the prevailing rock fO_2, to be further elaborated upon below.

The presence of homogeneous ilmenite in metaperidotites has previously been attributed to the partial breakdown of F-poor Ti-clinohumite (Trommsdorff & Evans, 1980; Trommsdorff *et al.*, 1998; López Sánchez-Vizcaíno *et al.*, 2005, 2009; Scambelluri *et al.*, 2014; Shen *et al.*, 2015), and calculated to occur between 620 and 640 °C (López Sánchez-Vizcaíno *et al.*, 2005, 2009). However, the stability of Ti-clinohumite depends on its fluorine content and, when F contents are high, its breakdown occurs at significantly higher temperatures (Weiss, 1997; Lopéz Sánchez-Vizcaíno *et al.*, 2009). As a consequence, partial breakdown of F-bearing Ti-clinohumite may well have occurred at peak conditions as the textures suggest. Bulk LA-ICP-MS measurements on hemo-ilmenite grains (Table 4) show enrichments in Nb (~270 μg g^{-1}) and, notably, similar Nb/Sc ratios compared with Ti-clinohumite (~1·2; Bretscher, 2017), strongly suggesting that hemo-ilmenite formed after Ti-clinohumite breakdown (Fig. 10c). Ilmeno-hematite grains, however, are present only in spinifex-textured Chl-harzburgites and are rimmed by ilmenite (Fig. 4d). This suggests that the composition of ilmeno-hematite grains may not have been equilibrated at peak *P*–*T* conditions; hence, ilmeno-hematite minerals may represent a transient feature generated at the onset of Ti-clinohumite breakdown that were then overgrown by ilmenite mantles in equilibrium with magnetite. If true, the ilmenite rims should not be accounted for when the pre-exsolution bulk ilmenite–hematite composition is determined. Another possibility for the formation of the ilmenite rims around ilmeno-hematite grains could be the protracted exsolution under prolonged cooling and

migration of Ti towards the crystal boundaries, as commonly observed in igneous rocks (Haggerty, 1976). In this case, the ilmenite rims also belong to the exsolution features and thus need to be accounted for when determining the pre-exsolution bulk ilmenite–hematite composition. Reintegration of 20–30 vol% of ilmenite rims, as estimated by image analysis (Fig. 10), would then slightly shift the bulk composition to a higher ilmenite component (0·47Ilm/0·53Hem to 0·53Ilm/0·47Hem, for 20 and 30 vol%, respectively) and to slightly lower Nb/Sc ratios (0·31–0·44). No matter how this reintegration is performed, the hematite–ilmenite compositions do not overlap between granular and spinifex-textured Chl-harzburgites (Fig. 10b).

It is difficult to obtain independent temperature and fO_2 estimates from the ilmenite–hematite solid solution minerals because hemo-ilmenite and ilmeno-hematite do not occur in the same lithology. In addition, the spinel and ulvöspinel components in magnetite are too low ($Al_2O_3 < 0{\cdot}5$ wt% and $TiO_2 < 0{\cdot}67$ wt%) to reliably employ the Fe–Ti geothermometer (Buddington & Lindsley, 1964; Ghiorso & Evans, 2008), best calibrated for much higher temperatures (800–1300 °C). Nevertheless, the low hematite component (average 0·81Ilm/0·19Hem) of hemo-ilmenite grains in the well-equilibrated granular-textured Chl-harzburgite, their coexistence with magnetite, the absence of hematite as individual grains, and the position of the ilmenite–hematite solvus below the magnetite–hematite (MH) buffer (Ghiorso & Sack, 1991; Ghiorso & Evans, 2008) all indicate that fO_2 conditions were well below the MH buffer at peak conditions, as has been concluded in previous work based on natural samples (Piccoli *et al.*, 2019), experiments (Iacovino *et al.*, 2020; Lazar, 2020) and pure modeling (Lazar, 2020).

Cr–V–Al–Fe^{3+} mass-balance modeling

A Cr–V–Al–Fe^{3+} mass balance is here employed to evaluate the fate of magnetite across the antigorite-breakdown reaction. As previously stated, the trivalent cations Cr, Fe^{3+}, Al, and V are essentially hosted in antigorite, chlorite and magnetite (Fig. 11), and antigorite is exhausted across the serpentine-dehydration reaction. Therefore, a Cr–V–Al–Fe^{3+} element distribution between magnetite and antigorite/chlorite can be used to assess whether the observed differences in modal amounts of magnetite in Atg-serpentinite and coexisting Chl-harzburgite at Almirez relate to consumption of magnetite during antigorite breakdown (e.g. Debret *et al.*, 2015; Merkulova *et al.*, 2016) or whether this represents a feature already acquired during seafloor alteration (Bretscher *et al.*, 2018). The model assumes a conservative behavior of Al, Fe^{3+}, Cr, and V (i.e. the bulk-rock concentrations of these elements remain constant across the antigorite dehydration reaction), and uses the Cr and V partition coefficients [e.g. $Kd_{Cr} = Cr_{(Mag)}/Cr_{(Atg\ or\ Chl)}$] calculated from measured data (see Supplementary Data S3 for additional details on the calculations). The partition coefficients of Cr and V between magnetite and antigorite in the Atg-serpentinite are 10–30 and 10–20, respectively, whereas in the Chl-harzburgite the partition coefficient between magnetite and chlorite is 10–20 for V and ~5 for Cr (Supplementary Data S3). As magnetite is the phase with the highest affinity for Cr and V, the concentrations of these elements in magnetite are a measure of its abundance for a given bulk-rock element concentration. In other words, increasing magnetite modes lead to progressively lower Cr and V concentrations in magnetite and vice versa.

Mass-balance calculations were done in two directions: (1) starting from the measured Atg-serpentinite, the Chl-harzburgite assemblage was calculated, maintaining the above-mentioned element partitioning between chlorite and magnetite; (2) starting from the measured Chl-harzburgite, the Atg-serpentinite protolith was back-calculated accordingly.

Aluminum is dominantly hosted in antigorite in serpentinite (Supplementary Data S3 Fig. S1) that makes up 80–90 vol% of the bulk-rock, whereas it is exclusively contained in 20–25 vol% of chlorite in Chl-harzburgite. This strong reduction in the amount of sheet silicates means that the ferric iron hosted in antigorite cannot all be incorporated into new chlorite. Assuming that the excess ferric iron is used to produce new magnetite, the mass of new magnetite formed can be obtained and this result tested against the redistribution of V and Cr liberated from antigorite upon breakdown into product chlorite and magnetite (olivine and orthopyroxene are irrelevant as a host; Bretscher, 2017).

The model results show that the amount of magnetite increases from the Atg-serpentinite to the Chl-harzburgite, irrespective of the direction of the calculations (open blue and red circles above the 1:1 line in Fig. 13a). In Atg-serpentinite, the observed magnetite mode ranges between 3·5 and 5·5 wt% (pale blue lines in Fig. 13a). Upon antigorite breakdown the amount of magnetite would increase to 5·8–7·8 wt%. In the Chl-harzburgite, the observed magnetite mode ranges between 1·5 and 2·5 wt% (pale red lines in Fig. 13a). The corresponding protolith serpentinite would have had only between 0 and 1·1 wt% magnetite. Sensitivity testing of the Cr–V–Al–Fe^{3+} mass-balance calculation was performed to explore how the calculated mineral modes react to using (1) different antigorite and chlorite $X Fe^{3+}$ values (dashed open circles in Fig. 13b) and (2) different V and Cr partition coefficients (different open circles in Figs 13a, b and 14). Figure 13b illustrates that variations in Cr and V partition coefficients have subordinate effects on magnetite modes, whereas variations in $X Fe^{3+}$ of antigorite and chlorite cause some more variability. However, irrespective of these uncertainties our inference remains that magnetite modes always increase from Atg-serpentinite to its partially dehydrated product Chl-harzburgite. Therefore, assuming fluid-immobility of Al, Fe^{3+}, Cr and V, magnetite mode in all the Chl-harzburgite samples investigated is far too low

to be generated by the dehydration of the coexisting Atg-serpentinites at Cerro del Almirez.

The mismatch between modeled and observed magnetite modes in the Chl-harzburgite samples can be possibly explained by the following: (1) loss of iron in the released aqueous fluids; (2) reduction of Fe^{3+} to Fe^{2+} with mass conservation of the bulk Fe_{tot} (magnetite modes are mainly controlled by the availability of Fe^{3+}; see Supplementary Data S3); (3) initial protolith heterogeneities. Although, with our present state of knowledge, there are no known aqueous complexes that could contribute to the transport of Fe^{3+}, previous isotopic studies suggested that Fe can be mobilized in aqueous fluids in the form of $Fe^{2+}Cl_2$ or $Fe^{2+}SO_x$ (Debret *et al.*, 2016). However, significant Fe^{2+} mobility would require high chlorine concentration, inconsistent with data from natural samples (e.g. Scambelluri *et al.*, 2004), and recent thermodynamic models predict only very low amount of Fe in serpentinite-derived fluids (Debret & Sverjensky, 2017). Hence, the hypothesis that the lower modal abundance of the observed magnetite compared with the model prediction is due to iron loss from the system after reduction of Fe^{3+} is excluded. For the second hypothesis to work, the predicted 5·8–7·8 wt% magnetite (forward model result from the Atg-serpentinite dehydration) would have to be reduced to 1·5 and 2·5 wt% magnetite as observed in the Chl-harzburgite. As magnetite contains 69 wt% Fe_2O_3 this would translate into a relatively large conversion of 3–3·7 wt% Fe_2O_3 to FeO, which could then be incorporated into product olivine and orthopyroxene. This would lower the Mg# of product olivine and orthopyroxene from a value of 94–95 (coexisting with 5·8–7·8 wt% magnetite) to 90–91. Such zoning is not observed in olivine and orthopyroxene of the Chl-harzburgite. In the granular Chl-harzburgite olivine Mg# varies in a small range from 89·5 to 90·5 whereas in the spinifex-textured Chl-harzburgite olivine Mg# increases slightly from 88–89 to 90·5–91·5 (Bretscher *et al.*, 2018). Thus, compositions of the coexisting silicate minerals do not document consumption of magnetite across the antigorite dehydration reaction. Therefore, in agreement with what has previously been proposed by Bretscher *et al.* (2018), we conclude that Atg-serpentinites and Chl-harzburgites had initially different magnetite contents, probably acquired during different extents of peridotite seafloor hydration and alteration. Indeed, the significant variation in the produced magnetite values (ΔMag; Fig. 13a) between samples can be related to variable modal magnetite/serpentine ratios produced on the ocean floor, intrinsically controlled by their degree of serpentinization (e.g. Bach *et al.*, 2006; Andreani *et al.*, 2013).

Figure 14 compares the mass-balance calculated equilibrium V and Cr compositions of magnetite in the Chl-harzburgite and the Atg-serpentinites with the corresponding measured concentrations. It can be seen

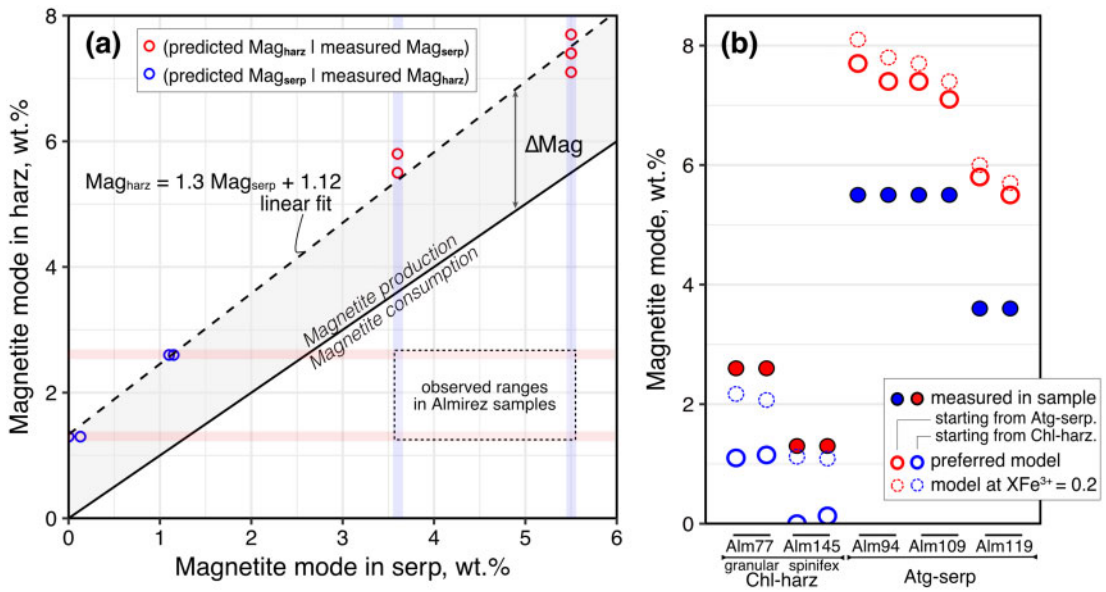

Fig. 13. Magnetite mode Cr–V–Al–Fe^{3+} mass-balance results. (a) Modeled relation between magnetite modes in Chl-harzburgite (harz) vs Atg-serpentinite (serp). Red symbols represent predicted amount of magnetite in Chl-harzburgite, starting from the measured magnetite modes in Atg-serpentinite (blue bands). Blue symbols represent predicted amount of magnetite in Atg-serpentinite, back-calculated from the measured magnetite modes in Chl-harzburgite (red bands). The continuous black line represents the 1:1 line along which magnetite is neither consumed nor produced during antigorite dehydration. The grey dashed line represents the linear regression for the modeled data; ΔMag represents the amount of magnetite produced during this reaction. Rectangle represents the compositional range observed in Almirez samples. (b) Magnetite modes for each Atg-serpentinite and Chl-harzburgite measured (filled circles)–modeled (open circles) pair. Red and blue symbols represent Chl-harzburgite and Atg-serpentinite samples, respectively. The preferred model employed given *K*d values for Cr and V combined with $XFe^{3+} = 0{\cdot}48$ and 0·50 for antigorite and chlorite, respectively (Debret *et al.*, 2015). The dashed circles represent the same model but using $XFe^{3+} = 0{\cdot}20$ for both minerals (compare Maurice *et al.*, 2020). It should be noted that for all these modeled examples, the magnetite modes in Chl-harzburgite are higher than in its corresponding Atg-serpentinite, thus implying magnetite production during the antigorite dehydration reaction. (See Supplementary Data S3 for more details.)

that there is a minimal change in Cr and V contents from the measured magnetite in the Atg-serpentinites (filled blue circles) to new magnetite in modeled Chl-harzburgites (open red circles; it should be recalled that different values are a result of using different *K*d values in the calculation) as they largely overlap. In contrast, the much lower amount of magnetite observed in the Chl-harzburgite goes along with significantly higher measured V and Cr concentrations. Concentrations of Cr and V calculated via mass balance for magnetite in modeled precursor Atg-serpentinite do not overlap with any of the measured magnetite textural types in the Atg-serpentinites. This comparison between measured and modeled Cr–V concentrations in magnetite from Atg-serpentinite demonstrates that initial heterogeneities between the Atg-serpentinites and the Chl-harzburgites existed and the first cannot be used as a precursor of the second.

The theoretical bulk magnetite composition predicted by the linear fit (or equilibrium co-variance) through modeled and measured bulk Cr and V as a function of modal magnetite is shown by a dashed line in Fig. 14a. This linear fit is overall consistent with trends in measured magnetite data but runs oblique to core–rim variation trends displayed by individual measurement points (Fig. 14b). This can be explained by measurements of volumetrically small growth-stages; for example, Mag-3 and Mag-5 cores (see also Fig. 6). Mag-5 cores might preserve the evidence of a local bulk effect, at high V and Cr concentrations released from antigorite at the onset of its breakdown reaction. With the progress of the reaction, while chlorite, olivine and orthopyroxene crystallize, they will take up V, Cr, Mg and Mn (Figs 6 and 9d), consequently decreasing their availability and concentration in magnetite. Magnetite concentrations will then approach conditions close to the bulk magnetite composition predicted by the linear fit (e.g. rims of Mag-5, and Mag-6 in granular-textured Chl-harzburgite, and both Mag-5 and Mag-6 in spinifex-textured Chl-harzburgite). Therefore, the observed zoning of Mag-5 is best explained by continuous magnetite growth in a small divariant field between the orthopyroxene-in and antigorite-out boundaries, between ~650 and ~670 °C (Bretscher *et al.*, 2018). An interesting aspect of this observation is that there is a dynamic increase in Mg# in the coexisting silicates when magnetite is produced during the antigorite breakdown reaction; this probably results in a widening of the divariant field by 10–20 °C where antigorite, chlorite, orthopyroxene, olivine and magnetite coexist. However, the conclusions for peak metamorphic conditions, bracketed by stability of antigorite in a high Mg# bulk (~96) and olivine + orthopyroxene in the lower Mg# bulk (92·7) of Bretscher *et al.* (2018) are not affected by this as the metamorphic constraints for the Atg-serpentinites and Chl-harzburgite are based on the actual measured magnetite content in each rock type.

MAGNETITE STABILITY AT HP CONDITIONS: IMPLICATIONS FOR THE REDOX STATE OF SUBDUCTING ULTRAMAFIC ROCKS

Our study provides detailed petrographic and *in situ* geochemical evidence demonstrating that magnetite is not only passively preserved across the antigorite-breakdown reaction (Bretscher *et al.*, 2018) but that new magnetite can indeed be formed as a reaction product from antigorite dehydration. In contrast, the experimental study of Merkulova *et al.* (2016) suggested that significant amounts of magnetite are consumed during the antigorite dehydration reaction. However, these piston cylinder experiments used a reducing assembly that caused H diffusion into the capsule and reduction from ferric to ferrous iron. Hence, these experiments have limited applicability to Almirez rocks, where the fluid is rock-buffered by the coexistence of olivine–orthopyroxene–magnetite and no evidence for magnetite consumption could be identified. Indeed, mass-balance calculations imply that new magnetite needs to form upon antigorite dehydration to accommodate the excess Fe^{3+} liberated from antigorite. In addition, despite reported differences in bulk-rock S (Alt *et al.*, 2012) between Atg-serpentinites and Chl-harzburgites from Almirez, no prominent mobilization of S is verified as pentlandite is stable in both Atg-serpentinite and Chl-harzburgite, in textural equilibrium with the peak temperature mineral assemblage including magnetite. This again highlights the prominent initial compositional variability of serpentinites, thus precluding direct compositional comparison between Atg-serpentinite and Chl-harzburgite, even when they coexist at the same locality as in Almirez.

Another apparent conflict exists between results of experimental work by Maurice *et al.* (2020) and our field-based data and thermodynamic modeling (Piccoli *et al.*, 2019; Iacovino *et al.*, 2020; Lazar, 2020). The experimental work of Maurice *et al.* (2020) employed a strongly oxidized starting material. With their multi-anvil experiments, they showed that when olivine had a Mg# higher than 95, hematite occurred together with magnetite in the run products, thus implying an fO_2 of 3–4 log units above the quartz–fayalite–magnetite buffer (QFM). In contrast, thermodynamic modeling by Piccoli *et al.* (2019), Iacovino *et al.* (2020) and Lazar (2020) reported a maximum 1–2 log units above QFM reached after antigorite decomposition employing a less oxidized harzburgitic bulk serpentinite composition, well below stability of hematite. In fact, this apparent conflict can be reconciled by looking at the equilibrium controlling fO_2 in the Chl-harzburgite [equation (4)]:

$$6\text{Fayalite} + 1O_2 = 3\text{Hedenbergite} + 2\text{Magnetite}. \quad (4)$$

The position of the buffer depends on the Mg# of olivine and orthopyroxene (generally equal at high temperature) and the composition of magnetite. As there are 6 moles of fayalite on the reactant side whereas there are only 3 moles of hedenbergite on the product

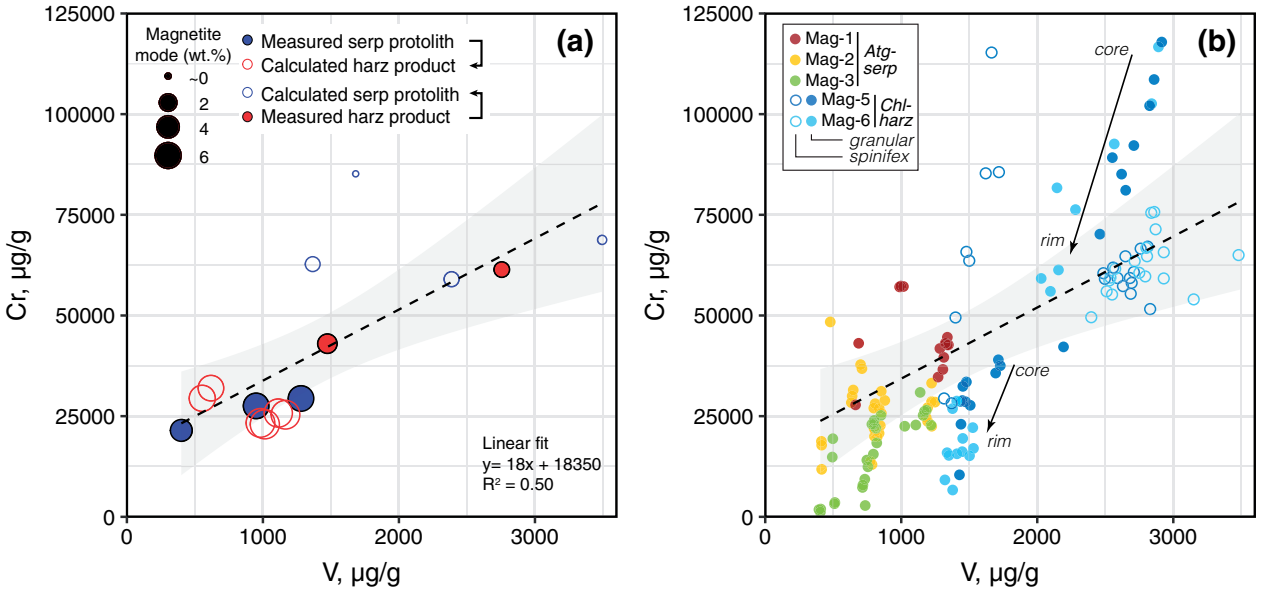

Fig. 14. Comparison of measured magnetite compositions with those calculated from Cr–V(–Al–Fe^{3+}) mass balance for predicted harzburgite (Chl-harz) product given the measured serpentinite protolith (Atg-serp), and vice versa. (a) Cr vs V bulk magnetite contents in measured (filled circles) and predicted (open circles) compositions for serpentinites (blue circles)–harzburgites (red circles). The size of the symbol represents the respective sample magnetite mode (in wt%). Dashed line represents the linear regression fit applied to the modeled and measured data (all plotted circles), with its one standard deviation shown as a grey shaded area. (b) Overlap of the calculated fit for bulk magnetite composition obtained in (a) to the individual magnetite spot measurement data. Arrows show core–rim evolution as measured in Mag-5.

side, the oxygen fugacity will increase with increasing Mg# of olivine. Dilution of magnetite iron by incorporation of Cr will shift the equilibrium to lower fO_2. For an Mg# of 90 for olivine and orthopyroxene and high-Cr (Cr_2O_3 < 10 wt%) magnetite as encountered in Chl-harzburgite at Almirez, the equilibrium results in an fO_2 of ~1 log unit above QFM at the antigorite dehydration reaction (Piccoli *et al.*, 2019; Lazar, 2020). On the other hand, the model of Evans & Frost (2021) for a magnetite-rich serpentinite bulk composition (Mg# = 96·4) resulted in an olivine Mg# of 97–98 and fO_2 of 4 log units above QFM. Together, this suggests that the Mg# of the silicates coexisting with magnetite in ultramafic rocks matters, whereby high amounts of magnetite cause high Mg# of coexisting silicates such as antigorite or olivine that then effect a shift to higher fO_2 of the bulk system.

The Mg# of olivine in Chl-harzburgite from Almirez cluster between 89 and 91 (Bretscher *et al.*, 2018), thus corresponding to the magnetite-poor case of Evans & Frost (2021). This also applies for the calculations of Piccoli *et al.* (2019), Iacovino *et al.* (2020) and Lazar (2020), which are therefore more relevant for Almirez Chl-harzburgite, yielding an fO_2 at ~1–2 log units above QFM. It is interesting to note that the Mg# of peak olivine in the spinifex-textured Chl-harzburgite (90·5–91·5) is slightly higher than in the granular Chl-harzburgite (89·5–90·5; Bretscher *et al.*, 2018). This might provide an explanation for the presence of hemo-ilmenite in the granular-type and ilmeno-hematite in the spinifex-type Chl-harzburgite. The composition of the Ti-bearing oxide phase will depend on the fertility of the serpentinite (bulk Ti content) and the Mg# of the bulk silicates, which in turn depends on the amount of magnetite in the bulk-rock.

The effect of Cr in magnetite was not considered in the calculations by Evans & Frost (2021). High amounts of Cr in magnetite will shift fO_2 to lower values (Piccoli *et al.*, 2019). Our study shows that Cr content of magnetite is inversely correlated with the amount of magnetite. Thus, magnetite-poor ultramafic rocks have a lower Mg# in coexisting silicates along with Cr-rich magnetite, resulting in a ΔfO_2 at 0–1, whereas magnetite-rich ultramafic rocks will have a higher Mg# in coexisting silicates along with Cr-poor magnetite leading to an fO_2 at 3–4 log units above QFM.

The magnetite-rich serpentinites at Almirez did not undergo the antigorite dehydration reaction. Our modeling predicts that Chl-harzburgites that derive from the breakdown of such serpentinites would have 5·8–7·8 wt% magnetite, resulting in a Mg# in the coexisting silicates that is even higher than that modeled by Bretscher *et al.* (2018) and corresponding to the 'oxidized case' modeled by Evans & Frost (2021). The expected Mg# of olivine produced upon antigorite dehydration is of the order of 95–97, corresponding to an fO_2 = 4 log units above QFM; that is, in the range of the hematite–magnetite buffer. Thus, in rocks with very high silicate Mg#, coexisting magnetite and hematite may occur. The modeling of Evans & Frost (2021) further suggests that under such high fO_2 the SO_2–H_2S equal activity line is probably crossed, thus offering the

opportunity to transfer redox budget in the form of SO_2 to the mantle wedge. More studies on ultramafic rocks with high-Mg# olivine and orthopyroxene are needed to assess whether sulfides are stable under these more oxidized conditions, to address the relevance of this process.

Altogether, the fO_2 heavily depends on the Mg# of the silicates coexisting with magnetite, which in turn depends on the amount of magnetite in the precursor serpentinite and the amount of magnetite produced during dehydration reactions. Our considerations show that there is a wide range of possible fO_2 at the antigorite dehydration reaction, and strong redox gradients are likely to exist within the same ultramafic body as inherited from oceanic peridotite hydration processes (Bretscher *et al.*, 2018). The Cr, V, and Al contents of magnetite in conjunction with Mg# of olivine and orthopyroxene in a single sample thus offer a quick and powerful method to infer whether a de-serpentinization fluid was more reduced or more oxidized.

Finally, our data show that the redox budget along with some fluid-mobile and redox-sensitive elements carried by magnetite and sulfides (e.g. Fe, Cr, Zn, Co, V, Ti, Sn, and W) can be transported within the subducting slab to depths greater than required for Atg-breakdown, notably for less oxidized ultramafic rocks. The question then arises whether some redox budget can be liberated at greater depths (e.g. when magnetite disappears upon chlorite dehydration; Piccoli *et al.*, 2019), or if other mechanisms are more relevant for the rather oxidized nature of arc magmas (e.g. Burgisser & Scaillet, 2007; Brounce *et al.*, 2014; Tollan & Hermann, 2019).

ACKNOWLEDGEMENTS

We are grateful for thoughtful reviews from Kayla Iacovino and two anonymous reviewers, and for efficient editorial handling by Sarah Sherlock. We thank P. Lanari, E. Kempf, and T. Bovay for setting up and assisting with the electron probe measurements at the University of Bern, and E. Reusser for helping and providing access to the electron probe at the ETH-Zurich. Finally, we also thank the Spanish authorities for providing the permit for fieldwork in the Sierra Nevada National Park.

FUNDING

This work was supported by the Swiss National Science Foundation (project No. 200021_172688) to T.P. and (project No. 206021_170722) to D. Rubatto and T.P.

DATA AVAILABILITY STATEMENT

The data underlying this article are available in the Zenodo Repository, at https://doi.org/10.5281/zenodo.4593408

SUPPLEMENTARY DATA

Supplementary data are available at *Journal of Petrology* online.

REFERENCES

Agrinier, P. & Cannat, M. (1997). Oxygen-isotope constraints on serpentinization processes in ultramafic rocks from the Mid-Atlantic Ridge (23°N). In: Karson, J. A., Cannat, M., Miller, D. J. & Elthon, D. (eds) *Proceedings of the Ocean Drilling Program, Scientific Results 153*. College Station, TX: Ocean Drilling Program, pp. 381–388.

Alt, J. C., Garrido, C. J., Shanks, W. C., Turchyn, A., Padrón-Navarta, J. A., López Sánchez-Vizcaíno, V., Gómez Pugnaire, M. T. & Marchesi, C. (2012). Recycling of water, carbon, and sulfur during subduction of serpentinites: a stable isotope study of Cerro del Almirez, Spain. *Earth and Planetary Science Letters* **327–328**, 50–60.

Andreani, M., Muñoz, M., Marcaillou, C. & Delacour, A. (2013). μXANES study of iron redox state in serpentine during oceanic serpentinization. *Lithos* **178**, 70–83.

Bach, W., Paulick, H., Garrido, C. J., Ildefonse, B., Meurer, W. P. & Humphris, S. E. (2006). Unraveling the sequence of serpentinization reactions: petrography, mineral chemistry, and petrophysics of serpentinites from MAR 15°N (ODP Leg 209, Site 1274). *Geophysical Research Letters* **33**, L13306.

Beard, J. S., Frost, B. R., Fryer, P., McCaig, A., Searle, R., Ildefonse, B., Zinin, P. & Sharma, S. K. (2009). Onset and progression of serpentinization and magnetite formation in olivine-rich troctolite from IODP Hole U1309D. *Journal of Petrology* **50**, 387–403.

Bina, M. M. & Henry, B. (1990). Magnetic properties, opaque mineralogy and magnetic anisotropies of serpentinized peridotites from ODP Hole 670A near the Mid-Atlantic Ridge. *Physics of the Earth and Planetary Interiors* **65**, 88–103.

Blakely, R. J., Brocher, T. M. & Wells, R. E. (2005). Subduction-zone magnetic anomalies and implications for hydrated forearc mantle. *Geology* **33**, 445–448.

Bonnemains, D., Carlut, J., Escartín, J., Mével, C., Andreani, M. & Debret, B. (2016). Magnetic signatures of serpentinization at ophiolite complexes. *Geochemistry, Geophysics, Geosystems* **17**, 2969–2986.

Bretscher, A. (2017). Trace element distribution and fluid chemistry during subduction related antigorite breakdown. PhD thesis, University of Bern.

Bretscher, A., Hermann, J. & Pettke, T. (2018). The influence of oceanic oxidation on serpentinite dehydration during subduction. *Earth and Planetary Science Letters* **499**, 173–184.

Brounce, M. N., Kelley, K. A. & Cottrell, E. (2014). Variations in $Fe^{3+}/\sum Fe$ of Mariana Arc Basalts and Mantle Wedge fO_2. *Journal of Petrology* **55**, 2513–2536.

Brounce, M. N., Kelley, K. A., Cottrell, E. & Reagan, M. K. (2015). Temporal evolution of mantle wedge oxygen fugacity during subduction initiation. *Geology* **43**, 775–778.

Buddington, A. F. & Lindsley, D. H. (1964). Iron–titanium oxide minerals and synthetic equivalents. *Journal of Petrology* **5**, 310–357.

Burgisser, A. & Scaillet, B. (2007). Redox evolution of a degassing magma rising to the surface. *Nature* **445**, 194–197.

Cannat, M. (1993). Emplacement of mantle rocks in the seafloor at mid-ocean ridges. *Journal of Geophysical Research: Solid Earth* **98**, 4163–4172.

Cannat, M., Bideau, D. & Bougault, H. (1992). Serpentinized Peridotites and Gabbros In the Mid-atlantic Ridge Axial

Valley At 15°37′N and 16°52′N. *Earth and Planetary Science Letters* **109**, 87–106.

Carbonin, S., Martin, S., Tumiati, S. & Rossetti, P. (2015). Magnetite from the Cogne serpentinites (Piemonte ophiolite nappe, Italy). Insights into seafloor fluid–rock interaction. *European Journal of Mineralogy* **27**, 31–50.

Colás, V., Padrón-Navarta, J. A., González-Jiménez, J. M., Griffin, W. L., Fanlo, I., O'Reilly, S. Y., Gervilla, F., Proenza, J. A., Pearson, N. J. & Escayola, M. P. (2016). Compositional effects on the solubility of minor and trace elements in oxide spinel minerals: Insights from crystal–crystal partition coefficients in chromite exsolution. *American Mineralogist* **101**, 1360–1372.

Connolly, J. A. D. & Thompson, A. B. (1989). Fluid and enthalpy production during regional metamorphism. *Contributions to Mineralogy and Petrology* **102**, 347–366.

Dare, S., Barnes, S. J. & Beaudoin, G. (2012). Variation in trace element content of magnetite crystallized from a fractionating sulfide liquid, Sudbury, Canada: Implications for provenance discrimination. *Geochimica et Cosmochimica Acta* **88**, 27–50.

Dare, S. A. S., Barnes, S. J., Beaudoin, G., Méric, J., Boutroy, E. & Potvin-Doucet, C. (2014). Trace elements in magnetite as petrogenetic indicators. *Mineralium Deposita* **49**, 785–796.

Debret, B. & Sverjensky, D. A. (2017). Highly oxidising fluids generated during serpentinite breakdown in subduction zones. *Scientific Reports* **7**, 10351.

Debret, B., Bolfan-Casanova, N., Padrón-Navarta, J. A., Martin-Hernandez, F., Andreani, M., Garrido, C. J., López Sánchez-Vizcaíno, V., Gómez-Pugnaire, M. T., Muñoz, M. & Trcera, N. (2015). Redox state of iron during high-pressure serpentinite dehydration. *Contributions to Mineralogy and Petrology* **169**, 36.

Debret, B., Millet, M.-A., Pons, M.-L., Bouilhol, P., Inglis, E. & Williams, H. (2016). Isotopic evidence for iron mobility during subduction. *Geology* **44**, 215–218.

Dupuis, C. & Beaudoin, G. (2011). Discriminant diagrams for iron oxide trace element fingerprinting of mineral deposit types. *Mineralium Deposita* **46**, 319–335.

Dyment, J., Arkani-Hamed, J. & Ghods, A. (1997). Contribution of serpentinized ultramafics to marine magnetic anomalies at slow and intermediate spreading centres: insights from the shape of the anomalies. *Geophysical Journal International* **129**, 691–701.

Evans, B. W. (2004). The serpentinite multisystem revisited: chrysotile is metastable. *International Geology Review* **46**, 479–506.

Evans, B. W. (2008). Control of the products of serpentinization by the $Fe^{2+}Mg_{-1}$ exchange potential of olivine and orthopyroxene. *Journal of Petrology* **49**, 1873–1887.

Evans, B. W. & Frost, B. R. (1975). Chrome-spinel in progressive metamorphism—a preliminary analysis. *Geochimica et Cosmochimica Acta* **39**, 959–972.

Evans, K. A. & Frost, B. R. (2021). Deserpentinization in subduction zones as a source of oxidation in arcs: a reality check. *Journal of Petrology* **62**, egab016.

Evans, B. W. & Trommsdorff, V. (1970). Regional metamorphism of ultramafic rocks in the Central Alps: parageneses in the system $CaO–MgO–SiO_2–H_2O$. *Schweizerische Mineralogische und Petrographische Mitteilungen* **50**, 481–492.

Evans, B. W., Dyar, M. D. & Kuehner, S. M. (2012). Implications of ferrous and ferric iron in antigorite. *American Mineralogist* **97**, 184–196.

Evans, K. A., Reddy, S. M., Tomkins, A. G., Crossley, R. J. & Frost, B. R. (2017). Effects of geodynamic setting on the redox state of fluids released by subducted mantle lithosphere. *Lithos* **278**, 26–42.

Frost, B. R. (1991). Stability of oxide minerals in metamorphic rocks. In: Lindsley, D. H. (ed.) *Oxide Minerals: Petrologic and Magnetic Significance, Mineralogical Society of America, Reviews in Mineralogy* **25**, 469–487.

Garcia-Casco, A., Torres-Roldan, R. L., Millan, G., Monie, P. & Schneider, J. (2002). Oscillatory zoning in eclogitic garnet and amphibole, Northern Serpentinite Melange, Cuba: a record of tectonic instability during subduction? *Journal of Metamorphic Geology* **20**, 581–598.

Ghiorso, M. & Sack, R. (1991). Fe-Ti Oxide geothermometry: Thermodynamic formulation and and the estimation of intensive variables in silicic magmas. *Contributions to Mineralogy and Petrology* **108**, 485–510.

Gerya, T. & Stöckhert, B. (2006). Two-dimensional numerical modeling of tectonic and metamorphic histories at active continental margins. *International Journal of Earth Sciences* **95**, 250–274.

Ghiorso, M. S. (1990). Thermodynamic properties of hematite–ilmenite–geikielite solid solutions. *Contributions to Mineralogy and Petrology* **104**, 645–667.

Ghiorso, M. S. & Evans, B. W. (2008). Thermodynamics of rhombohedral oxide solid solutions and a revision of the Fe–Ti two-oxide geothermometer and oxygen-barometer. *American Journal of Science* **308**, 957–1039.

Haggerty, S. E. (1976). Opaque mineral oxides in terrestrial igneous rocks. In: Rumble, D. (ed.) *Oxide Minerals, Mineralogical Society of America, Reviews in Mineralogy* **3**, 89–112.

Hellstrom, J., Paton, C., Woodhead, J. & Hergt, J. (2008). Laser ablation ICP–MS in the earth sciences: current practices and outstanding issues. In: Sylvester, P. (ed.) *Laser Ablation ICP–MS in the Earth Sciences: Current Practices and Outstanding Issues. Mineralogical Association of Canada, Short Course Series* **40**, 343–348.

Iacovino, K., Guild, M. R. & Till, C. B. (2020). Aqueous fluids are effective oxidizing agents of the mantle in subduction zones. *Contributions to Mineralogy and Petrology* **175**, 36.

Kelley, K. A. & Cottrell, E. (2009). Water and the oxidation state of subduction zone magmas. *Science* **325**, 605–607.

Kempf, E., Hermann, J., Reusser, E., Baumgartner, L. & Lanari, P. (2020). The role of the antigorite + brucite to olivine reaction in subducted serpentinites (Zermatt, Switzerland). *Swiss Journal of Geosciences* **113**.

Klein, F., Bach, W., Humphris, S. E., Kahl, W.-A., Jons, N., Moskowitz, B. & Berquo, T. S. (2014). Magnetite in seafloor serpentinite—some like it hot. *Geology* **42**, 135–138.

Kodolányi, J., Pettke, T., Spandler, C., Kamber, B. S. & Gméling, K. (2012). Geochemistry of ocean floor and fore-arc serpentinites: constraints on the ultramafic input to subduction zones. *Journal of Petrology* **53**, 235–270.

Laborda-López, C., López-Sánchez-Vizcaíno, V., Marchesi, C., Gómez-Pugnaire, M. T., Garrido, C. J., Jabaloy-Sánchez, A., Padrón-Navarta, J. A. & Hidas, K. (2018). High-*P* metamorphism of rodingites during serpentinite dehydration (Cerro del Almirez, Southern Spain): implications for the redox state in subduction zones. *Journal of Metamorphic Geology* **36**, 1141–1173.

Lanari, P. & Engi, M. (2017). Local bulk composition effects on metamorphic mineral assemblages. In: Kohn, M. J., Engi, M. & Lanari, P. (eds) *Petrochronology: Methods and Applications. Mineralogical Society of America, Reviews in Mineralogy And Geochemistry* **83**, 55–102.

Lanari, P., Vidal, O., De Andrade, V., Dubacq, B., Lewin, E., Grosch, E. G. & Schwartz, S. (2014). XMapTools: a MATLAB©-based program for electron microprobe X-ray

image processing and geothermobarometry. *Computers & Geosciences* **62**, 227–240.

Lanari, P., Vho, A., Bovay, T., Airaghi, L. & Centrella, S. (2019). Quantitative compositional mapping of mineral phases by electron probe micro-analyser. In: Ferrero, S., Lanari, P., Gonçalves, P. & Grosch, E. G. (eds) *Metamorphic Geology: Microscale to Mountain Belts, Geological Society, London, Special Publications* **478**, 39–63.

Lazar, C. (2020). Using silica activity to model redox-dependent fluid compositions in serpentinites from 100 to 700 °C and from 1 to 20 kbar. *Journal of Petrology* **61**, 1–25.

López Sánchez-Vizcaíno, V., Gómez-Pugnaire, M. T., Trommsdorff, V., Müntener, O. & Rubatto, D. (2001). Middle Miocene high-pressure metamorphism and fast exhumation of the Nevado–Filabride Complex, SE Spain. *Terra Nova* **13**, 327–332.

López Sánchez-Vizcaíno, V., Trommsdorff, V., Gómez-Pugnaire, M. T. T., Garrido, C. J., Müntener, O. & Connolly, J. A. D. (2005). Petrology of titanian clinohumite and olivine at the high-pressure breakdown of antigorite serpentinite to chlorite harzburgite (Almirez Massif, S. Spain). *Contributions to Mineralogy and Petrology* **149**, 627–646.

López Sánchez-Vizcaíno, V., Gómez-Pugnaire, M. T., Garrido, C. J., Padrón-Navarta, J. A. & Mellini, M. (2009). Breakdown mechanisms of titanclinohumite in antigorite serpentinite (Cerro del Almirez massif, S. Spain): a petrological and TEM study. *Lithos* **107**, 216–226.

Lyubetskaya, T. & Ague, J. J. (2009). Modeling the magnitudes and directions of regional metamorphic fluid flow in collisional orogens. *Journal of Petrology* **50**, 1505–1531.

Maffione, M., Morris, A., Plümper, O., &. & van Hinsbergen, D. J. J. (2014). Magnetic properties of variably serpentinized peridotites and their implication for the evolution of oceanic core complexes. *Geochemistry, Geophysics, Geosystems* **15**, 923–944.

Martin, W., Baross, J., Kelley, D. & Russell, M. J. (2008). Hydrothermal vents and the origin of life. *Nature Reviews, Microbiology* **6**, 805–814.

Maurice, J., Bolfan-Casanova, N., Demouchy, S., Chauvigne, P., Schiavi, F. & Debret, B. (2020). The intrinsic nature of antigorite breakdown at 3 GPa: experimental constraints on redox conditions of serpentinite dehydration in subduction zones. *Contributions to Mineralogy and Petrology* **175**, 94.

Merkulova, M., Muñoz, M., Vidal, O. & Brunet, F. (2016). Role of iron content on serpentinite dehydration depth in subduction zones: Experiments and thermodynamic modeling. *Lithos* **264**, 441–452.

Ménez, B., Pisapia, C., Andreani, M., Jamme, F., Vanbellingen, Q. P., Brunelle, A., Richard, L., Dumas, P. & Réfrégiers, M. (2018). Abiotic synthesis of amino acids in the recesses of the oceanic lithosphere. *Nature* **564**, 59–63.

Mothersole, F. E., Evans, K. & Frost, B. R. (2017). Abyssal and hydrated mantle wedge serpentinised peridotites: a comparison of the 15°20′N fracture zone and New Caledonia serpentinites. *Contributions to Mineralogy and Petrology* **172**, 69.

Oufi, O., Cannat, M. & Horen, H. (2002). Magnetic properties of variably serpentinized abyssal peridotites. *Journal of Geophysical Research* **107**, 2095.

Padrón-Navarta, J. A., Hermann, J., Garrido, C. J. L., Sánchez-Vizcaíno, V. & Gómez-Pugnaire, M. T. (2010). An experimental investigation of antigorite dehydration in natural silica-enriched serpentinite. *Contributions to Mineralogy and Petrology* **159**, 25–42.

Padrón-Navarta, J. A., Lopez Sanchez-Vizcaino, V., Garrido, C. J. & Gomez-Pugnaire, M. T. (2011). Metamorphic record of high-pressure dehydration of antigorite serpentinite to chlorite harzburgite in a subduction setting (Cerro del Almirez, Nevado–Filabride Complex, Southern Spain). *Journal of Petrology* **52**, 2047–2078.

Palme, H. & O'Neill, H. (2014). Cosmochemical estimates of mantle composition. In: Holland, H. D. & Turekian, K. K. (eds) Earth Systems and Environmental Sciences, *Treatise on Geochemistry*, 2nd edn., Volume 3. Amsterdam: Elsevier, pp. 1–39.

Paton, C., Hellstrom, J., Paul, B., Woodhead, J. & Hergt, J. (2011). Iolite: freeware for the visualisation and processing of mass spectrometric data. *Journal of Analytical Atomic Spectrometry* **26**, 2508–2518.

Peters, D. & Pettke, T. (2017). Evaluation of major to ultra trace element bulk rock chemical analysis of nanoparticulate pressed powder pellets by LA-ICP-MS. *Geostandards and Geoanalytical Research* **41**, 5–28.

Peters, D., Bretscher, A., John, T., Scambelluri, M. & Pettke, T. (2017). Fluid-mobile elements in serpentinites: Constraints on serpentinisation environments and element cycling in subduction zones. *Chemical Geology* **466**, 654–666.

Peters, D., Pettke, T., John, T. & Scambelluri, M. (2020). The role of brucite in water and element cycling during serpentinite subduction—Insights from Erro Tobbio (Liguria, Italy). *Lithos* **360–361**, 105431.

Pettke, T., Oberli, F., Audétat, A., Guillong, M., Simon, A. C., Hanley, J. J. & Klemm, L. M. (2012). Recent developments in element concentration and isotope ratio analysis of individual fluid inclusions by laser ablation single and multiple collector ICP-MS. *Ore Geology Reviews* **44**, 10–38.

Piccoli, F., Hermann, J., Pettke, T., Connolly, J. A. D., Kempf, E. D. & Vieira Duarte, J. F. (2019). Subducting serpentinites release reduced, not oxidized, aqueous fluids. *Scientific Reports* **9**, 1–7.

Puga, E., Nieto, J., Dı'az de Federico, A., Bodinier, J. & Morten, L. (1999). Petrology and metamorphic evolution of ultramafic rocks and dolerite dykes of the Betic Ophiolitic Association (Mulhacén Complex, SE Spain). *Lithos* **49**, 23–56.

Ranero, C. R., Phipps Morgan, J., McIntosh, K. & Reichert, C. (2003). Bending-related faulting and mantle serpentinization at the Middle America trench. *Nature* **425**, 367–373.

Sack, R. O. & Ghiorso, M. S. (1991). Chromian spinels as petrogenetic indicators: thermodynamics and petrological applications. *American Mineralogist* **76**, 827–847.

Scambelluri, M., Hoogerduijn-Strating, E. H., Piccardo, G. B., Vissers, R. L. M. & Rampone, E. (1991). Alpine olivine- and titanian clinohumite-bearing assemblages in the Erro–Tobbio peridotite (Voltri Massif, NW Italy). *Journal of Metamorphic Geology* **9**, 79–91.

Scambelluri, M., Rampone, E. & Piccardo, G. B. (2001). Fluid and element cycling in subducted serpentinite: a trace-element study of the Erro–Tobbio high-pressure ultramafites (Western Alps, NW Italy). *Journal of Petrology* **42**, 55–67.

Scambelluri, M., Fiebig, J., Malaspina, N., Müntener, O. & Pettke, T. (2004). Serpentinite subduction: implications for fluid processes and trace-element recycling. *International Geology Review* **46**, 595–613.

Scambelluri, M., Pettke, T., Rampone, E., Godard, M. & Reusser, E. (2014). Petrology and trace element budgets of high-pressure peridotites indicate subduction dehydration of serpentinized mantle (Cima di Gagnone, Central Alps, Switzerland). *Journal of Petrology* **55**, 459–498.

Schneider, C. A., Rasband, W. S. & Eliceiri, K. W. (2012). NIH Image to ImageJ: 25 years of image analysis. *Nature Methods* **9**, 671–675.

Schönbächler, M. (1999). Die Hochdruckmetamorphose der Ultramafika und der angrenzenden Nebengesteine am Cerro de Almirez, Sierra Nevada, Südspanien. Diplomarbeit, ETH Zürich.

Schwartz, S., Guillot, S., Reynard, B., Lafay, R., Debret, B., Nicollet, C., Lanari, P. & Auzende, A. L. (2013). Pressure–temperature estimates of the lizardite/antigorite transition in high pressure serpentinites. *Lithos* **178**, 197–210.

Seyfried, W. E., Foustoukos, D. I. & Fu, Q. (2007). Redox evolution and mass transfer during serpentinization: an experimental and theoretical study at 200°C, 500 bar with implications for ultramafic-hosted hydrothermal systems at Mid-Ocean Ridges. *Geochimica et Cosmochimica Acta* **71**, 3872–3886.

Shen, T., Hermann, J., Zhang, L., Lü, Z., Padrón-Navarta, J. A., Xia, B. & Bader, T. (2015). UHP Metamorphism documented in Ti-chondrodite- and Ti-clinohumite-bearing serpentinized ultramafic rocks from Chinese Southwestern Tianshan. *Journal of Petrology* **56**, 1425–1458.

Sleep, N. H., Meibom, A., Fridriksson, T., Coleman, R. G. & Bird, D. K. (2004). H_2-rich fluids from serpentinization: geochemical and biotic implications. *Proceedings of the National Academy of Sciences of the USA* **101**, 12818–12823.

Toffolo, L., Nimis, P., Martin, S., Tumiati, S. & Bach, W. (2017). The Cogne magnetite deposit (Western Alps, Italy): a Late Jurassic seafloor ultramafic-hosted hydrothermal system? *Ore Geology Reviews* **83**, 103–126.

Toft, P. B., Arkani-Hamed, J. & Haggerty, S. E. (1990). The effects of serpentinization on density and magnetic susceptibility: a petrophysical model. *Physics of the Earth and Planetary Interiors* **65**, 137–157.

Tollan, P. & Hermann, J. (2019). Arc magmas oxidized by water dissociation and hydrogen incorporation in orthopyroxene. *Nature Geoscience* **12**, 667–671.

Trommsdorff, V. & Evans, B. W. (1980). Titanian hydroxyl-clinohumite: Formation and breakdown in antigorite rocks (Malenco, Italy). *Contributions to Mineralogy and Petrology* **72**, 229–242.

Trommsdorff, V., López Sánchez-Vizcaíno, V., Gómez-Pugnaire, M. T. & Müntener, O. (1998). High pressure breakdown of antigorite to spinifex-textured olivine and orthopyroxene. *Contributions to Mineralogy and Petrology* **132**, 139–148.

Vitale Brovarone, A., Sverjensky, D. A., Piccoli, F., Ressico, F., Giovannelli, D. & Daniel, I. (2020). Subduction hides high-pressure sources of energy that may feed the deep subsurface biosphere. *Nature Communications* **11**, 3880.

Weiss, M. (1997). Clinohumites: a field and experimental study. PhD thesis, ETH Zurich.

Whitney, D. L. & Evans, B. W. (2010). Abbreviations for names of rock-forming minerals. *American Mineralogist* **95**, 185–187.

Whittaker, E. J. W. & Wicks, F. J. (1970). Chemical differences among the serpentine "polymorphs": a discussion. *American Mineralogist* **55**, 1025–1047.